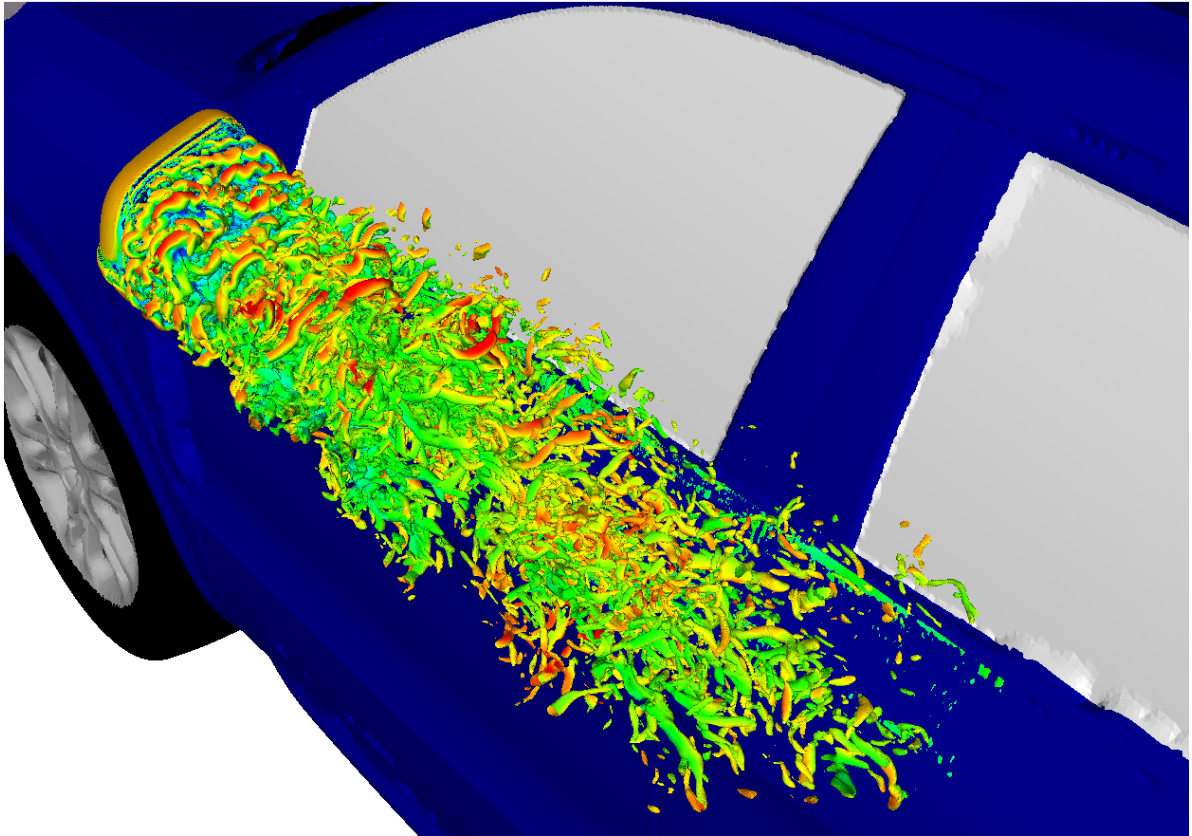




CHALMERS
UNIVERSITY OF TECHNOLOGY



Joint Optimization of Aerodynamics and Aeroacoustics of Side View Mirrors

Master's thesis in Engineering Mathematics and Computational Science

MATTIAS STRIDH

MASTER'S THESIS 2018:32

Joint Optimization of Aerodynamics and Aeroacoustics of Side View Mirrors

Mattias Stridh



CHALMERS
UNIVERSITY OF TECHNOLOGY

Department of Mechanics and Maritime Sciences
Division of Fluid Dynamics
CHALMERS UNIVERSITY OF TECHNOLOGY
Gothenburg, Sweden 2018

Joint Optimization of Aerodynamics and Aeroacoustics of Side View Mirrors
Mattias Stridh

© Mattias Stridh, 2018.

Examiner: Lars Davidson, Department of Mechanics and Maritime Sciences

Master's Thesis 2018:32
Department of Mechanics and Maritime Sciences
Division of Fluid Dynamics
Chalmers University of Technology
SE-412 96 Gothenburg
Telephone +46 31 772 1000

Cover: Illustration of the vortices in the wake of the side mirror by an iso-surface of the Q-criterion at $2 \cdot 10^6$ coloured with the total pressure.

Chalmers Reproservice
Gothenburg, Sweden 2018

Joint Optimization of Aerodynamics and Aeroacoustics of Side View Mirrors
Mattias Stridh
Department of Mechanics and Maritime Sciences
Division of Fluid Dynamics
Chalmers University of Technology

Abstract

This thesis is carried out at China Euro Vehicle Technology (CEVT) and aims at developing a method for performing multidisciplinary optimization for automotive applications. Such applications could be to optimize side mirrors, a-pillars, spoilers etc. for disciplines such as aerodynamics, aeroacoustics, contamination etc. For this thesis the optimization is performed in terms of aerodynamics and aeroacoustics on the side view mirrors of a passenger car. Another part of the thesis is to investigate the possibilities to post process and analyse the results, in order to find and understand the design parameters and how they affect the different disciplines. Two design parameters are used in the study. One parameter is the position of the mirror along the car and the other is the angle between the side of the car and the inside of the mirror. The optimization procedure follows four steps. The geometry is first morphed in the pre processing program ANSA into the design that will be simulated. A surface mesh is saved as a geometry representation. The second step is that the surface mesh is loaded into FLUENT meshing which creates the simulation domain and the volume mesh. Step two is performed in two separate session simultaneously, one for the aerodynamic and one for the aeroacoustic simulations. The next step is that the volume mesh is read by FLUENT which simulates the flow and calculates the optimization parameters, drag for the aerodynamic simulations and sound pressure level for the aeroacoustic simulations. The final step is that the optimization program HEEDS determines the new morphing parameters to send to ANSA based on the results from the previous simulations. A bash script was written which reads the design parameters from a separate file and runs ANSA and FLUENT in the correct order. HEEDS changes the design parameters in this separate file and then runs the bash script to obtain the output variables. After the output is obtained the process starts over. It was found that the angle of the inside of the mirror should be increased slightly to reduce drag and SPL. The optimal choice of the x-position seemed to be outside of the investigated interval, moving the mirror as far back on the car as possible was best in terms of drag. The effect the x-position had on the noise on the side window was very small.

Keywords: Aeroacoustics, Aerodynamics, CFD, DES, Drag, MDO, SPL

Acknowledgements

This master's thesis was carried out at China Euro Vehicle Technology, CEVT. First of all I would like to thank my supervisor Jari Kesti at CEVT for the help, tips and discussions. This help was a great factor in carrying out this thesis successfully. Thank you also to Sofia Ore who gave me the opportunity to come to CEVT and performing thesis. I am also grateful for the help and support that was always available from the other close colleagues at CEVT, Samuel Gabriel, Anders Karlsson, Simon Lindberg, Leon Löwered and Mattias Olander.

I would also like to thank Andrés Contreras and Neeti Shetty who were also doing their master's theses at CEVT at the same time as me. Discussions and conversations with both of them was of great value throughout the thesis. Since they experienced similar challenges as me from how the microwave worked, to report writing and meshing issues.

Furthermore I would like to thank Lars Davidson, my examiner at Chalmers, for taking his time to be the examiner of my thesis.

Mattias Stridh, Gothenburg, June 2018

Nomenclature

Acronyms

BOI	Body of Influence
CEVT	China Euro Vehicle Technology
CFD	Computational Fluid Dynamics
DDES	Delayed Detached Eddy Simulations
DES	Detached Eddy Simulations
FW-H	Ffowcs Williams and Hawkings
LES	Large Eddy Simulations
MDO	Multidisciplinary Design Optimization
OEM	Original Equipment Manufacturer
RANS	Reynolds-averaged Navier-Stokes
SPL	Sound Pressure Level
URANS	Unsteady Reynolds-averaged Navier-Stokes
WALE	Wall-Adapting Local Eddy-Viscosity

Physical quantities and variables

C_D	Drag coefficient	1
C_L	Lift coefficient	1
δ_{ij}	Kronecker delta	1
δ	Dirac delta function	1
ϵ	Turbulent dissipation rate	m^2/s^3
F_D	Drag force	kgm/s^2
F_L	Lift force	kgm/s^2
H	Heaviside function	1
k	Turbulent kinetic energy	m^2/s^2
κ	Thermal conductivity	$\text{kg m}/\text{s}^3\text{K}$
μ	Dynamic viscosity	$\text{kg}/\text{m s}$
ν_t	Turbulent viscosity (for RANS)	m^2/s
ν_{sgs}	Turbulent viscosity (for LES)	m^2/s
ω	Specific rate of dissipation	$1/\text{s}$
p	Pressure	$\text{kg}/\text{m s}^2$
ρ	Density	kg/m^3
τ_{ij}	Viscous stress tensor	$\text{kg}/\text{m s}^2$
θ	Temperature	K
u	Internal energy	$\text{kg m}^2/\text{s}^2$
v_i	Velocity in the i direction	m/s
v_∞	Free stream velocity	m/s
V	Cell Volume	m^3

Mattias Stridh, Gothenburg, June 2018

Contents

1	Introduction	1
1.1	Background	1
1.2	Project Description	1
1.2.1	Purpose	2
1.2.2	Aim	2
1.2.3	Limitations	2
2	Theory	3
2.1	Aerodynamics	3
2.2	Fluid Dynamics	3
2.3	Turbulence modelling	4
2.3.1	RANS	5
2.3.1.1	$k - \epsilon$ model	5
2.3.1.2	$k - \omega$ model	6
2.3.1.3	$k - \omega$ SST model	6
2.3.2	URANS	7
2.3.3	LES	8
2.3.4	DES	8
2.3.4.1	DDES	9
2.4	Acoustics	9
2.4.1	A-weighting	11
2.4.2	Acoustic Analogy	12
2.5	Optimization	14
3	Method	17
3.1	Geometry	17
3.2	Aerodynamics	19
3.2.1	Mesh	19
3.2.2	Case	21
3.3	Aeroacoustics	21
3.3.1	Mesh	21
3.3.2	Case	22
3.4	Optimization	23
4	Results and Discussion	25
4.1	Optimized design	25

4.2	Aerodynamic results	26
4.3	Aeroacoustic results	29
4.4	Optimization results	32
5	Conclusion	37
5.1	Future work	37
	Bibliography	39
A	Simulation times and frequency limits	I
B	Correlation plots	V

1

Introduction

Since the introduction of computers in the automotive industry decades ago the use of simulations has grown and keeps growing. Simulations to estimate the drag on the car have been performed for many years, although still being improved. Wind generated noise has also been estimated using computers for many years. It is however not until recent years it has become feasible to run optimisation between multiple disciplines for full scale car models with accuracy and within a reasonable time. This chapter gives a brief background to the project and a description of the project including purpose, aim and limitations.

1.1 Background

With the rapid development of technology and increased awareness of the environment come higher demands on performance, comfort, carbon dioxide emissions etc. The car industry is no exception and has high demands on, for example, fuel consumption and noise levels from both customers and legal requirements. The fuel consumption can be lowered by reducing the drag force on the vehicle which is highly dependent on the exterior shape of the vehicle. External and internal noise levels are also dependent on the shape of the vehicle as wind induced noise can be a big part of the overall noise especially at higher velocities. To meet the demands, Original Equipment Manufacturers (OEMs) use Computational Fluid Dynamics (CFD) to estimate the drag force and wind induced noise. CFD is of big importance in the automotive industry today as it gives opportunities to optimise the aerodynamics of the vehicles. This is both faster and cheaper than producing physical models and performing wind tunnel tests.

The CFD simulations used to optimise the drag and the wind generated noise are, in most cases, run independent of each other and the optimal solutions seldom coincide. Accurate simulations of the drag and noise are costly in terms of computer power, hence is it not feasible to simulate large numbers of different shapes of the vehicle and choose the optimal design. To find an optimal design without having to run a lot of simulations Multidisciplinary Design Optimisation (MDO) can be applied.

1.2 Project Description

The project is carried out at China Euro Vehicle Technology (CEVT) where CFD is utilised to estimate the drag force acting on the whole vehicle and the wind

generated noise at the front side window. The estimations will be computed for different configurations of the side view mirrors.

1.2.1 Purpose

The main purpose of the master thesis is to develop a method for performing MDO for automotive applications. The thesis will focus specifically on optimization between aerodynamics and aeroacoustics although the method should be versatile enough to introduce other disciplines such as contamination without an excessive amount of work.

Another purpose of the thesis is to gain understanding of important design parameters with regards to aerodynamics and aeroacoustics, focusing foremost on the side view mirrors. Knowing these parameters and how they affect each discipline respectively would be highly valuable as it would reduce the work it takes to find joint optimal solutions with respect to aerodynamics and aeroacoustics in the future.

1.2.2 Aim

The aim of the thesis is to develop an effective and versatile method for MDO between disciplines such as aerodynamics, aeroacoustics and contamination. The method should also work well for CEVT and be suited for their work flow. The method should, for example, be easy to understand and implement and not require installation of new software. Another part of the thesis is to analyse and understand different design parameters and how they affect the different disciplines.

1.2.3 Limitations

The time span of 20 weeks for the project led to the following limitations:

- Simulations are carried out for aerodynamics and aeroacoustics and not other disciplines such as contamination.
- The side view mirror is the only part that is being optimised.

The limitation in computational power led to the following limitations:

- The vehicle model that is used will be completely closed and have a flat underbody.
- A half vehicle model is used for the aeroacoustics simulations.
- Two parameters for the side view mirrors are being optimized.
- A limited frequency span is investigated in the aeroacoustics simulations.

2

Theory

The theory of the project is presented in this chapter. Aerodynamics and fluid dynamics is explained first followed by a section with turbulence modelling. The acoustics theory used in the project is explained next and the chapter closes with a section about optimization.

2.1 Aerodynamics

When driving a vehicle there are forces acting on it due to the surrounding air. The forces are created from friction between the air and the car and from pressure differences. There are two main components of the aerodynamic force that are of most interest when designing the exterior of a car. That is the drag force which is acting in the opposite direction of the vehicle's motion and the lift force which is perpendicular to the drag force and most often defined as positive in the upward direction. The drag force has a significant negative influence on the fuel consumption, especially at higher velocities. By modifying the geometry to make the vehicle more aerodynamic the drag force can be reduced heavily.

Dimensionless parameters are often used to measure the drag/lift force to compare different vehicle shapes. These parameters are called drag/lift coefficient and are defined as

$$C_{D/L} = \frac{2F_{D/L}}{\rho A v_{\infty}^2} \quad (2.1)$$

where $F_{D/L}$ is the drag/lift force, A is a suitable reference area, ρ is the density and v_{∞} is the free stream velocity [1].

2.2 Fluid Dynamics

A fluids motion is described by the equations of conservation, given that the fluid is valid under the continuum assumption. This assumes that measurable properties such as temperature, pressure and density are well-defined at infinitesimal volume elements. These elements are assumed to be large compared to individual fluid molecules but small compared to the characteristic length scales of the flow. The continuum assumption is valid for most common applications such as air flowing around a car.

The first of the equations of conservation is the continuity equation or conservation equation of continuity (2.2),

$$\frac{\partial \rho}{\partial t} + \frac{\partial \rho v_i}{\partial x_i} = 0. \quad (2.2)$$

The equation states that change of mass in a system is equal to the mass entering the system minus the mass leaving the system.

Next are the momentum equations or Navier-Stokes equations. The Navier-Stokes equations are three in total, one in each dimension (x, y, z in Cartesian coordinates). The equations are stated in (2.3) below, here body forces are neglected,

$$\begin{aligned} \frac{\partial \rho v_i}{\partial t} + \frac{\partial \rho v_i v_j}{\partial x_j} &= -\frac{\partial p}{\partial x_i} + \frac{\partial \tau_{ij}}{\partial x_j} \\ \tau_{ij} &= 2\mu S_{ij} - \frac{2}{3}\mu \frac{\partial v_k}{\partial x_k} \delta_{ij} \end{aligned} \quad (2.3)$$

where τ_{ij} is called the viscous stress tensor. The three momentum equations describe the motion of viscous fluids and the solution is a flow field in three dimensions.

The final conservation equation is the energy equation (2.4), where the radiation term has been neglected.

$$\frac{\partial \rho u}{\partial t} + \frac{\partial \rho v_i u}{\partial x_i} = -p \frac{\partial v_i}{\partial x_i} + 2\mu S_{ij} S_{ij} - \frac{2}{3}\mu S_{kk} S_{ii} + \frac{\partial}{\partial x_i} \left(\kappa \frac{\partial \theta}{\partial x_i} \right) \quad (2.4)$$

The energy equation states that no energy is created nor destroyed but transformed between different forms such as internal energy and kinetic energy.

In equations (2.2) to (2.4) ρ is the density, v_i is the velocity, p is pressure, μ is dynamic viscosity, $S_{ij} = \frac{1}{2} \left(\frac{\partial v_i}{\partial x_j} + \frac{\partial v_j}{\partial x_i} \right)$, κ is thermal conductivity, u is the internal energy and θ is temperature.

2.3 Turbulence modelling

Most typical fluid flows such as rivers, blood flow, wind around cars or air planes are turbulent. These flows feature a wide range of length and time scales which all influence each other. Because of this wide range of scales it is very computationally heavy to resolve all turbulence and modelling has to be done. The most common approach is to average the flow in a certain way. A widely used averaging technique is time averaging which results in the Reynolds-averaged Navier-Stokes (RANS) equations. All turbulent scales are modelled when this technique is used. Another averaging approach is volume averaging. This approach averages in space and the idea is to resolve the larger turbulent scales and model the smaller scales. Which scales are being resolved and modelled depends on how fine your computational mesh is. This technique is commonly known as Large Eddy Simulations (LES) and is more computationally expensive than RANS because it requires a finer mesh.

In this section all turbulence models that are relevant for the thesis are presented. Note that all equations are written in their incompressible form.

2.3.1 RANS

The RANS equations are the time-averaged Navier-Stokes equations. Replacing the velocities with the time-averaged and instantaneous velocities in the Navier-Stokes equations (2.3) and then time-averaging all the terms again result in the RANS equations. Using calculation rules for time-averaged and instantaneous variables, which can be found in [2], and assuming incompressibility and constant viscosity the RANS equations become

$$\rho \bar{v}_j \frac{\partial \bar{v}_i}{\partial x_j} = -\frac{\partial \bar{p}}{\partial x_i} + \frac{\partial}{\partial x_j} \left(\mu \frac{\partial \bar{v}_i}{\partial x_j} - \rho \overline{v'_i v'_j} \right) \quad (2.5)$$

where the bar means the time-averaged variable and the apostrophe means the instantaneous variable. The term $\rho \overline{v'_i v'_j}$ is called the Reynolds stress tensor and is symmetric. Hence are six unknowns introduced on top of the four other unknowns, pressure and three velocities. This is where the so called closure problem occurs. There are only four equations, the continuity equation and the three N-S equations. The energy equation is sometimes added to this although it introduces temperature as an unknown so the problem of having six unknowns still remain.

A common approach at dealing with the closure problem is to model the Reynolds stresses using the Boussinesq assumption. The Boussinesq assumption reduces the amount of unknown variables from six to two by introducing a turbulent viscosity, ν_t , and keeping the trace of the Reynolds stresses in the equation. This is done as

$$\overline{v'_i v'_j} = -\nu_t \left(\frac{\partial \bar{v}_i}{\partial x_j} + \frac{\partial \bar{v}_j}{\partial x_i} \right) + \frac{1}{3} \delta_{ij} \overline{v'_k v'_k}. \quad (2.6)$$

The second term on the right hand side is added to get a valid equation for the trace of the Reynolds stress tensor. Since if that term would not be added, by continuity, trace of the right hand side equal to zero but the left hand side would not equate to zero.

So called two equation models are often used to model the turbulent viscosity and the most common one is the $k - \epsilon$ model [3]. However there are many other two-equation models such as the $k - \omega$ model proposed by Wilcox [4] and the $k - \tau$ model proposed by Speziale et al [5]. Another widely used model is the Menter's Shear Stress Transport (SST) which is a combination of $k - \epsilon$ and $k - \omega$. This model uses the $k - \omega$ model in inner regions of the boundary layer and $k - \epsilon$ in the outer regions [6].

2.3.1.1 $k - \epsilon$ model

Turbulent kinetic energy is the trace of the Reynolds stress tensor divided by 2, i.e. $k = \frac{1}{2} \overline{v'_i v'_i}$. An equation for k can be derived by taking the trace of the Reynolds stress equation and dividing by 2. The k equation that is obtained contains additional unknowns which require modelling. After the modelling of the terms containing unknowns, the modelled k -equation becomes

$$\frac{\partial k}{\partial t} + \bar{v}_j \frac{\partial k}{\partial x_j} = \nu_t \left(\frac{\partial \bar{v}_i}{\partial x_j} + \frac{\partial \bar{v}_j}{\partial x_i} \right) \frac{\partial \bar{v}_i}{\partial x_j} + \frac{\partial}{\partial x_j} \left[\left(\nu + \frac{\nu_t}{\sigma_k} \right) \frac{\partial k}{\partial x_j} \right] - \epsilon \quad (2.7)$$

where the buoyancy term is not included for simplicity. The destruction term ϵ is a new unknown which require modelling. An equation for ϵ can be derived by looking at the k equation and making a similar equation for ϵ . This is done by replacing k with ϵ and scaling the terms that do not include the turbulent kinetic energy by the factor ϵ/k to get the correct dimensions.

$$\frac{\partial \epsilon}{\partial t} + \bar{v}_j \frac{\partial \epsilon}{\partial x_j} = c_{\epsilon 1} \frac{\epsilon}{k} \nu_t \left(\frac{\partial \bar{v}_i}{\partial x_j} + \frac{\partial \bar{v}_j}{\partial x_i} \right) \frac{\partial \bar{v}_i}{\partial x_j} + \frac{\partial}{\partial x_j} \left[\left(\nu + \frac{\nu_t}{\sigma_\epsilon} \right) \frac{\partial \epsilon}{\partial x_j} \right] - c_{\epsilon 2} \frac{\epsilon^2}{k}. \quad (2.8)$$

The turbulent viscosity introduced in Equation (2.6) is still unknown. The dimension of it is $[\text{m}^2/\text{s}]$. The turbulent viscosity can therefore be modelled as a product of the turbulent velocity and length scales. The velocity scale is estimated by $k^{1/2}$ and the length scale by $k^{3/2}/\epsilon$. This gives an expression for the turbulent viscosity as

$$\nu_t = c_\mu \frac{k^2}{\epsilon}. \quad (2.9)$$

The standard values for the coefficients ($c_\mu, c_{\epsilon 1}, c_{\epsilon 1}, c_k, c_\epsilon$) are through testing found to be (0.09, 1.44, 1.92, 1, 1.3) respectively.

2.3.1.2 $k - \omega$ model

The $k - \omega$ model is similar to the $k - \epsilon$ model although it utilises the specific rate of dissipation ω instead of the dissipation ϵ . The specific rate of dissipation is defined as $\omega \propto \epsilon/k$. The k -equation for the $k - \omega$ model looks like

$$\frac{\partial k}{\partial t} + \bar{v}_j \frac{\partial k}{\partial x_j} = \nu_t \left(\frac{\partial \bar{v}_i}{\partial x_j} + \frac{\partial \bar{v}_j}{\partial x_i} \right) \frac{\partial \bar{v}_i}{\partial x_j} + \frac{\partial}{\partial x_j} \left[\left(\nu + \frac{\nu_t}{\sigma_k^\omega} \right) \frac{\partial k}{\partial x_j} \right] - \beta^* \omega k. \quad (2.10)$$

This k -equation is the same k -equation as in the $k - \epsilon$ model, Equation (2.7). Except for the dissipation term where the definition of ω has been used, a constant has been added to the dissipation term and the constant σ is changed. The ω -equation is derived in the same manner as the ϵ -equation was derived in the $k - \epsilon$ model. Following the same procedure the ω -equation is obtained as

$$\frac{\partial \omega}{\partial t} + \bar{v}_j \frac{\partial \omega}{\partial x_j} = c_{\omega 1} \frac{\omega}{k} \nu_t \left(\frac{\partial \bar{v}_i}{\partial x_j} + \frac{\partial \bar{v}_j}{\partial x_i} \right) \frac{\partial \bar{v}_i}{\partial x_j} + \frac{\partial}{\partial x_j} \left[\left(\nu + \frac{\nu_t}{\sigma_\omega} \right) \frac{\partial \omega}{\partial x_j} \right] - c_{\omega 2} \omega^2. \quad (2.11)$$

The constants ($\sigma_k^\omega, \sigma_\omega, \beta^*, c_{\omega 1}$ and $c_{\omega 1}$) in Equation (2.10) and (2.11) are equal to (2, 2, 0.09, 5/9 and 3/40) respectively.

2.3.1.3 $k - \omega$ SST model

The $k - \omega$ SST model is a combination between the $k - \epsilon$ and the $k - \omega$ model. The $k - \epsilon$ is used in the free shear flow and $k - \omega$ is used in the inner boundary layer.

The equations take the following form

$$\begin{aligned}
 \frac{\partial k}{\partial t} + \bar{v}_j \frac{\partial k}{\partial x_j} &= \nu_t \left(\frac{\partial \bar{v}_i}{\partial x_j} + \frac{\partial \bar{v}_j}{\partial x_i} \right) \frac{\partial \bar{v}_i}{\partial x_j} + \frac{\partial}{\partial x_j} \left[\left(\nu + \frac{\nu_t}{\sigma_k} \right) \frac{\partial k}{\partial x_j} \right] - \beta^* \omega k \\
 \frac{\partial \omega}{\partial t} + \bar{v}_j \frac{\partial \omega}{\partial x_j} &= \alpha \left(\frac{\partial \bar{v}_i}{\partial x_j} + \frac{\partial \bar{v}_j}{\partial x_i} \right) \frac{\partial \bar{v}_i}{\partial x_j} + \frac{\partial}{\partial x_j} \left[\left(\nu + \frac{\nu_t}{\sigma_\omega} \right) \frac{\partial \omega}{\partial x_j} \right] - \beta \omega^2 \\
 &\quad + 2(1 - F_1) \frac{\sigma_{\omega 2}}{\omega} \frac{\partial k}{\partial x_j} \frac{\partial \omega}{\partial x_j}.
 \end{aligned} \tag{2.12}$$

Where the variable definitions are

$$\begin{aligned}
 F_1 &= \tanh(\xi^4), \quad \xi = \min \left[\max \left(\frac{\sqrt{k}}{\beta^* \omega d}, \frac{500\nu}{d^2 \omega} \right), \frac{4\sigma_{\omega 2} k}{CD_{k\omega} d^2} \right], \\
 CD_{k\omega} &= \max \left(2\sigma_{\omega 2} \frac{1}{\omega} \frac{\partial k}{\partial x_j} \frac{\partial \omega}{\partial x_j}, 10^{-10} \right), \\
 \nu_t &= \frac{a_1 k}{\max(a_1 \omega, |\bar{S}| F_2)}, \quad \bar{S} = \frac{1}{2} \left(\frac{\partial \bar{v}_i}{\partial x_j} + \frac{\partial \bar{v}_j}{\partial x_i} \right), \\
 F_2 &= \tanh(\eta^2), \quad \eta = \max \left(\frac{2\sqrt{k}}{\beta^* \omega d}, \frac{500\nu}{d^2 \omega} \right)
 \end{aligned} \tag{2.13}$$

and d is the distance to the closest wall. When $F_1 = 1$ the last term in the second equation in (2.12) becomes zero and the model behaves as the $k - \omega$ model and for $F_1 = 0$ the model behaves as the $k - \epsilon$ model. By looking at the expression for ξ in Equation (2.13) it can be seen that ξ grows as d gets smaller which in turn makes F_1 go towards one. That F_1 tends to one means that the behaviour of $k - \omega$ is obtained which is desired in the near wall region. The coefficients in the SST model is a mix of the $k - \epsilon$ and the $k - \omega$ model. The mix is determined using the function F_1 as

$$\phi = \phi_1 F_1 + \phi_2 (1 - F_1).$$

The constants are as follows

$$\begin{aligned}
 \sigma_{k1} &= 0.85 & \sigma_{k2} &= 1 & \sigma_{\omega 1} &= 0.5 & \sigma_{\omega 2} &= 0.856 \\
 \alpha_1 &= \frac{5}{9} & \alpha_2 &= 0.44 & \beta_1 &= \frac{3}{40} & \beta_2 &= 0.0828 \\
 \beta^* &= 0.09 & a_1 &= 0.3 & & & &
 \end{aligned}$$

2.3.2 URANS

Unsteady Reynolds-averaged Navier-Stokes (URANS) applies time-averaging for smaller intervals compared to averaging over all time as in RANS. The URANS averaging is written

$$\bar{v}_i(t) = \frac{1}{2T} \int_{t-T}^{t+T} v_i(t) dt \tag{2.14}$$

$$v_i = \bar{v}_i + v_i''$$

where v_i'' is the fluctuating velocity within the time-averaged interval. The URANS time-averaging gives similar momentum equations as RANS except for the fact that all of the variables are time-dependent.

$$\rho \frac{\partial \bar{v}_i}{\partial t} + \rho \bar{v}_j \frac{\partial \bar{v}_i}{\partial x_j} = -\frac{\partial \bar{p}}{\partial x_i} + \frac{\partial}{\partial x_j} \left(\mu \frac{\partial \bar{v}_i}{\partial x_j} - \overline{\rho v_i'' v_j''} \right). \quad (2.15)$$

The same turbulence models for the Reynolds stresses can be used in URANS as in RANS with the addition of time dependency [2].

2.3.3 LES

Large eddy simulations resolve the large eddies (the larger turbulent scales) of the flow and model the smaller eddies. The process to resolve the larger scales begins with, as for RANS, averaging of the N-S equations although in LES volume average is applied instead of time average.

After volume averaging of every term in the N-S equations is performed, the LES equations become

$$\rho \frac{\partial \bar{v}_i}{\partial t} + \rho \bar{v}_j \frac{\partial \bar{v}_i}{\partial x_j} = -\frac{\partial \bar{p}}{\partial x_i} + \frac{\partial}{\partial x_j} \left(\mu \frac{\partial \bar{v}_i}{\partial x_j} - \rho \tau_{ij} \right). \quad (2.16)$$

where $\tau_{ij} = \overline{v_i v_j} - \bar{v}_i \bar{v}_j$ together with the density give the sub grid stresses. For a more thorough derivation see [7].

A common way to model the subgrid stresses in LES is done in the same fashion as for RANS, via the Boussinesq assumption. Using this assumption τ_{ij} is expressed as

$$\tau_{ij} = -2\nu_{sgs} \bar{S}_{ij} + \frac{1}{3} \delta_{ij} \tau_{kk}. \quad (2.17)$$

A widely used model for the turbulent viscosity for the sub grid scales, ν_{sgs} , is the Wall-Adapting Local Eddy-Viscosity (WALE) model [8]. For the WALE model the turbulent viscosity is modelled as

$$\nu_{sgs} = L_s^2 \frac{\left(S_{ij}^d S_{ij}^d \right)^{3/2}}{\left(\bar{S}_{ij} \bar{S}_{ij} \right)^{5/2} + \left(S_{ij}^d S_{ij}^d \right)^{5/4}} \quad (2.18)$$

where L_s and S_{ij}^d are defined as

$$L_s = \min \left\{ \kappa d, C_w V^{1/3} \right\} \quad (2.19)$$

$$S_{ij}^d = \frac{1}{2} (\bar{g}_{ij}^2 + \bar{g}_{ji}^2) - \frac{1}{3} \delta_{ij} \bar{g}_{kk}^2, \quad \bar{g}_{ji} = \frac{\partial \bar{v}_i}{\partial x_j}.$$

2.3.4 DES

Detached Eddy Simulation (DES) is an approach using both URANS and LES. RANS is applied in the boundary layer and LES is employed in the outer region.

The boundary layer is strongly dependent on the unsteady flow in outer region hence will there be unsteady flow in the boundary layer as well which is why it is treated with URANS.

The momentum equations for URANS, Eq. (2.15), and LES, Eq. (2.16), look the same except for the notation of the turbulent viscosity (ν_t and ν_{sgs}) i.e.

$$\frac{\partial \bar{v}_i}{\partial t} + \bar{v}_j \frac{\partial \bar{v}_i}{\partial x_j} = -\frac{1}{\rho} \frac{\partial \bar{p}}{\partial x_i} + \frac{\partial}{\partial x_j} \left((\nu + \nu_{t/sgs}) \frac{\partial \bar{v}_i}{\partial x_j} \right). \quad (2.20)$$

Because the equations look the same for URANS and LES all that has to be controlled is the turbulent viscosity to switch between the models. The $k - \omega$ SST model is a common choice of model for the turbulent viscosity in DES.

Recall the $k - \omega$ SST model from Section 2.3.1.3. When running DES, the destruction term in the k -equation in Equation (2.12) is modified. A factor F_{DES} is added to the term in order to switch between RANS and LES. The switch is done through the turbulent length scale as

$$\begin{aligned} \beta^* k \omega &\rightarrow \beta^* k \omega F_{DES}, & F_{DES} &= \max \left(\frac{L_t}{C_{DES} \Delta}, 1 \right) \\ \Delta &= \max(\Delta x_1, \Delta x_2, \Delta x_3), & L_t &= \frac{k^{1/2}}{\beta^* \omega}. \end{aligned} \quad (2.21)$$

The function F_{DES} switches between the turbulent length scales $k^{1/2}/\omega$ and Δ for RANS and LES respectively. When F_{DES} becomes larger than one the model will go in to LES mode as the flow will be induced to go unsteady. With F_{DES} larger than one the dissipation of k will increase. This leads to a reduction of k which in turn reduces the turbulent viscosity. A smaller turbulent viscosity means that less turbulence is modelled and more is resolved which is the LES mode [2].

2.3.4.1 DDES

When performing DES simulations the model can switch to LES mode in the boundary layer with a mesh that is too coarse if the mesh is not carefully constructed in the near wall regions. Making this switch in the boundary layer means that the results will have bad accuracy because the mesh will be too coarse for accurate LES results. There are different ways to protect the boundary layer from being treated with LES. The most common way is to modify the blending function F_{DES} from Equation (2.21) as

$$F_{DES} = \max \left(\frac{L_t}{C_{DES} \Delta} (1 - F_{SST}), 1 \right) \quad (2.22)$$

where F_{SST} usually is chosen as either F_1 or F_2 defined in Equation (2.13) from the $k - \omega$ SST model. Performing this protection of the boundary layer is known as delayed detached eddy simulations (DDES) [2].

2.4 Acoustics

All sounds are pressure perturbations propagating as waves. The human ear can detect sound waves of a frequency between 20 HZ and 20 kHz, these sounds are

called acoustic. Sounds above this spectra are referred to as ultrasounds and sound waves with a frequency below 20 Hz are called infrasounds. A common way of measuring sound levels is through a logarithmic decibel scale. The Sound Pressure Level (SPL) is defined as

$$SPL = 10\log\left(\frac{p_{rms}^2}{p_0^2}\right) = 20\log\left(\frac{p_{rms}}{p_0}\right) \quad (2.23)$$

where p_{rms} is the root-mean-square sound pressure and p_0 is the reference sound pressure [9]. The sound pressure is the difference between the pressure in the sound wave and the averaged surrounding pressure. The p_{rms} is computed by taking the square of the sound pressure and averaging in time or space and taking the square root of the average. The reference pressure is commonly chosen as $p_0 = 2 \cdot 10^{-5}$ Pa in air which is approximately the threshold of hearing for the human ear. Because of the non linearity in Equation (2.23) the combined SPL value of several sources is calculated as

$$SPL_o = 10\log(10^{(source_1/10)} + 10^{(source_2/10)} + \dots + 10^{(source_n/10)}). \quad (2.24)$$

Aeroacoustic noise generation comes from three different mechanisms. The first mechanism is idealised by a monopole source and comes from unsteady volumetric flow. An example of this type of noise source is when you roll down the window in a driving car. Dipole sources originates from the interaction between rigid surfaces and fluctuating pressure. Unsteady pressures from separated flows such as von Kármán vortex shedding is an example of such a source. The dipole sources can be modelled by two monopole sources separated by a small distance oscillating out of phase. The final mechanism is the quadrupole. These sources can be modelled by two dipoles oscillating out of phase. The quadrupole sources are generated from unsteady internal stresses in a fluid, such as the ones from a jet flow [10]. The three sources all scale with the velocity of the flow and the Mach number differently. The sources scale as

$$\begin{aligned} I_{mono} &\propto \frac{\rho}{c} u^4 = \rho u^3 M \\ I_{di} &\propto \frac{\rho}{c^3} u^6 = \rho u^3 M^3 \\ I_{quadru} &\propto \frac{\rho}{c^5} u^8 = \rho u^3 M^5. \end{aligned} \quad (2.25)$$

Because quardupole sources scale with M^5 it is neglected for most cases with a low Mach number. Monopole sources are the most dominant source at low Mach numbers which is why preventing leaks into the car cabin should be prioritised when trying to reduce the noise inside a car. Provided that all leaks into the cabin are sealed the dipole sources should also be examined as the noise generated from the flow around parts like the a-pillar and side mirror can make a difference on the noise heard inside the cabin.

Octave bands are commonly used to analyse a source by frequencies. Sets of frequencies are called bands and are divided from a wide range of frequencies. A band has an octave width when the upper frequency of the band is twice the magnitude

of the lower band frequency. The octave bands have their nominal frequencies at 16, 31.5, 63, 125, 250, ..., 16000 Hz. To get the lower frequency limit of an octave band divide the nominal frequency with $\sqrt{2}$ and to get the upper limit multiply by $\sqrt{2}$, see Table 2.1.

2.4.1 A-weighting

The human hearing is not uniformly sensitive to sounds of all frequencies in the acoustic frequency domain (20 Hz to 20 kHz). The human ear is most sensitive to sounds with a frequency around 3 kHz. Because of this difference in sensitivity a sound with an SPL of 100 dB appears much louder if it has a frequency of 2000 Hz instead of 30 Hz [9]. To adjust for this difference and to be able to compare the perceived loudness of sounds with varying frequencies different weightings have been developed. A commonly used and simple weighting is the so called A-weighting. This function looks like

$$20 \log_{10} \left(\frac{12194^2 \cdot f^4}{(f^2 + 20.6^2) \sqrt{(f^2 + 107.7^2)(f^2 + 737.9^2)(f^2 + 12194^2)}} \right) + 2.00, \quad (2.26)$$

where f is the frequency and the output will be the adjustment to make to the decibel. The function is normalized at 1000 Hz. A table of the adjustments for the octave bands and a plot of the curve can be found in Table 2.1 and Figure 2.1 respectively.

Lower Frequency	Nominal Frequency	Upper Frequency	A-Weighting
11 Hz	16 Hz	22 Hz	-
22 Hz	31.5 Hz	44 Hz	-39.4 dB
44 Hz	63 Hz	44 Hz	-26.2 dB
88 Hz	125 Hz	177 Hz	-16.1 dB
177 Hz	250 Hz	355 Hz	-8.6 dB
355 Hz	500 Hz	710 Hz	-3.2 dB
710 Hz	1000 Hz	1420 Hz	0 dB
1420 Hz	2000 Hz	2840 Hz	1.2 dB
2840 Hz	4000 Hz	5680 Hz	1 dB
5680 Hz	8000 Hz	11360 Hz	-1.1 dB
11360 Hz	16000 Hz	22720 Hz	-6.6 dB

Table 2.1: Table of octave bands and their A-weighting adjustments.

As seen by the a-weighting values in Table 2.1 both small and large frequencies are weighted down and the frequencies around 2.5 kHz are weighted up. It is also seen that the human ear is more sensitive to the largest frequencies compared to the smallest frequencies.

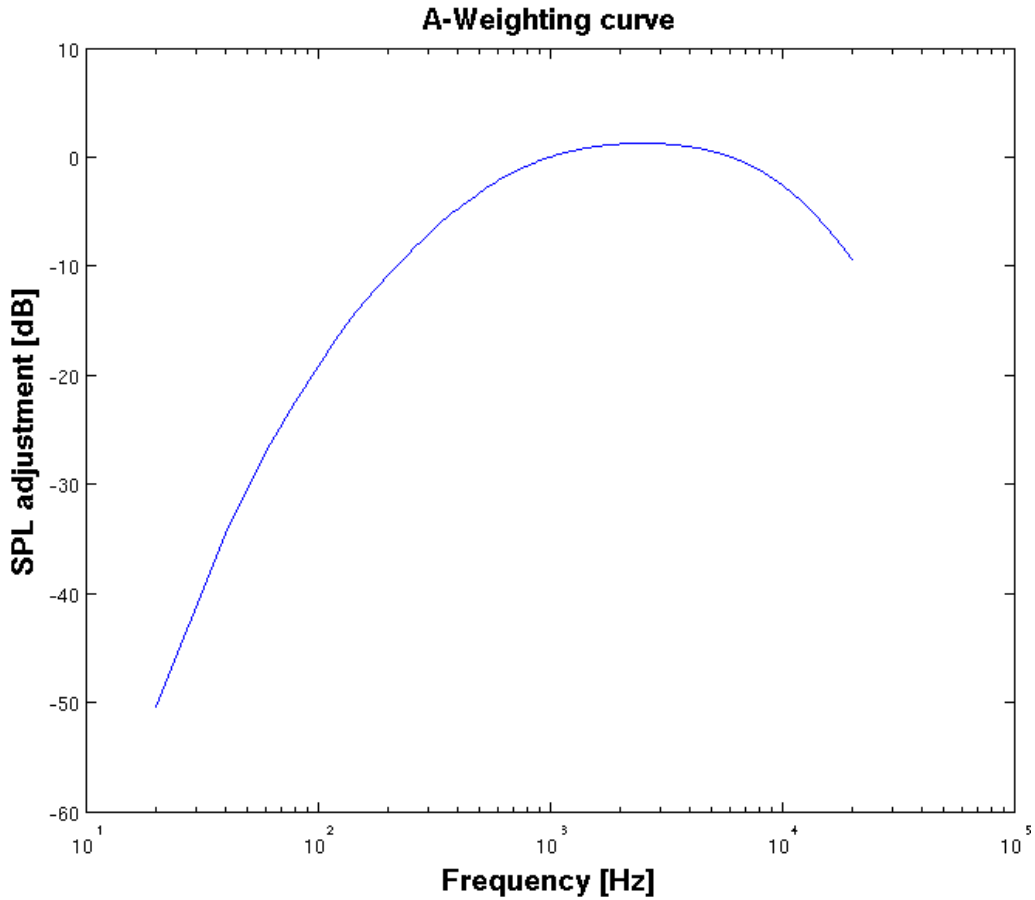


Figure 2.1: A-Weighting curve

2.4.2 Acoustic Analogy

In order to solve flow induced generation of sound the governing equations would have to be solved together with the propagation of the sound. This is extremely computationally heavy and not practical in engineering applications. This is the reason why acoustic analogies have been developed. These analogies decouple the flow and the acoustic waves. First the flow is solved using a transient simulation such as LES or DES. The flow variables are then used in the acoustic analogies. Since the flow and the acoustics are decoupled the sound waves are not affecting the flow.

One of the first analogies was the so called Lighthill's analogy [11]. The Lighthill's wave equation governing the pressure perturbations is derived from the continuity and from the Navier-Stokes equations. The continuity equation and the N-S equations are found in Equation (2.2) and (2.3). Subtract the divergence of the momentum equation from the time derivative of the continuity equation to obtain

$$\frac{\partial^2 \rho}{\partial t^2} = \frac{\partial^2}{\partial x_i \partial x_j} (\rho v_i v_j + p \delta_{ij} - \tau_{ij}). \quad (2.27)$$

By subtracting $c_0^2 \frac{\partial^2 \rho}{\partial x_i^2}$ from Equation (2.27) the Lighthill's equation is obtained

$$\begin{aligned} \frac{\partial^2 \rho}{\partial t^2} - c_0^2 \frac{\partial^2 \rho}{\partial x_i^2} &= \frac{\partial^2 T_{ij}}{\partial x_i \partial x_j} \\ T_{ij} &= \rho v_i v_j + (p - \rho c_0^2) \delta_{ij} - \tau_{ij} \end{aligned} \quad (2.28)$$

where T_{ij} is called the Lighthill tensor. The Lighthill's equation is an inhomogeneous wave equation. It is also an exact equation as no assumptions have been made in the derivation. Outside the turbulent regions the pressure and density act as for a quiescent fluid as the perturbations would be small. These small perturbations would also be governed by the homogeneous wave equation in this region. If the velocity of the flow is assumed to be zero the Lighthill's equation does in fact boil down to the homogeneous wave equation as the right hand side in Equation (2.28) would vanish. The pressure and density perturbations can be expressed through a reference pressure p_0 and density ρ_0 , equivalent to that of a quiescent fluid, as

$$p' = p - p_0 \quad \rho' = \rho - \rho_0. \quad (2.29)$$

The Lighthill's equation becomes

$$\frac{\partial^2 \rho'}{\partial t^2} - c_0^2 \frac{\partial^2 \rho'}{\partial x_i^2} = \frac{\partial^2 T_{ij}}{\partial x_i \partial x_j}. \quad (2.30)$$

The Lighthill equation can be solved analytically using the Green's function. The solution looks like

$$\rho'(\mathbf{x}, t) = \frac{1}{4\pi c_0^2} \int_V \frac{1}{r} \frac{\partial^2 T_{ij}}{\partial x_i \partial x_j}(\mathbf{y}, t - \frac{r}{c_0}) d\mathbf{y} \quad (2.31)$$

where \mathbf{x} is the receiver location, \mathbf{y} is the source location and $r = |\mathbf{x} - \mathbf{y}|$ is the distance between them. The density and pressure fluctuations have the relation

$$\rho'(\mathbf{x}, t) = \frac{1}{c_0^2} p'(\mathbf{x}, t) \quad (2.32)$$

if the propagation of the sound waves is assumed to be an adiabatic process. By combining the solution in Equation (2.31) with the relation in Equation (2.32) the far field pressure fluctuations can be obtained and used to compute the SPL from Equation (2.23).

The Lighthill's analogy was extended by Curle [12] to account for the effect of stationary walls and further extended later by Ffowcs Williams and Hawkings (FW-H)[13] to include the effect of moving walls.

The generalized Lighthill's equation derived by FW-H takes the form

$$\begin{aligned} \frac{\partial^2 H(f) \rho'}{\partial t^2} - c_0^2 \frac{\partial^2 H(f) \rho'}{\partial x_i^2} &= \frac{\partial^2 H(f) T_{ij}}{\partial x_i \partial x_j} + \frac{\partial}{\partial x_i} \{ [\rho v_i (v_n - u_n) + (p' \delta_{ij} - \tau_{ij}) n_j] \delta(f) \} \\ &+ \frac{\partial}{\partial t} \{ [\rho (v_n - u_n) + \rho_0 u_n] \delta(f) \} \end{aligned} \quad (2.33)$$

where v is the fluid velocity, u is the surface velocity, δ is the Dirac delta function, H is the Heaviside function and n is the unit normal vector of the wall.

Two terms have been added on the right hand side of the Lighthill's equation (2.28) in the FW-H formulation. The second term on the right hand side in FW-H's equation (2.33) is the term accounting for stationary walls and the last term is the term accounting for moving walls, these two terms are only nonzero on a wall as $f = 0$ on the wall. The FW-H is often expressed in integral form which consists of volume and surface integrals where the volume integrals correspond to quadropole sources and can be neglected for small Mach numbers. If the volume integrals are dropped the solution becomes

$$p'(\mathbf{x}, t) = p'_T(\mathbf{x}, t) + p'_L(\mathbf{x}, t)$$

where

$$\begin{aligned} 4\pi p'_T(\mathbf{x}, t) &= \int_{f=0} \left[\frac{\rho_0(\dot{U}_n + U_{\dot{n}})}{r(1 - M_r)^2} \right] dS \\ &+ \int_{f=0} \left[\frac{\rho_0 U_n (r \dot{M}_r + c_0(M_r - M^2))}{r^2(1 - M_r)^3} \right] dS \\ 4\pi p'_L(\mathbf{x}, t) &= \frac{1}{c_0} \int_{f=0} \left[\frac{\dot{L}_r}{r(1 - M_r)^2} \right] dS \\ &+ \int_{f=0} \left[\frac{L_r - L_M}{r^2(1 - M_r)^2} \right] dS \\ &+ \int_{f=0} \left[\frac{L_r (r \dot{M}_r + c_0(M_r - M^2))}{r^2(1 - M_r)^3} \right] dS. \end{aligned} \tag{2.34}$$

The expressions for L and U are

$$\begin{aligned} U_i &= u_i + \frac{\rho}{\rho_0} (v_i - u_i) \\ L_i &= (p' \delta_{ij} - \tau_{ij}) n_j + \rho v_i (v_n - u_n). \end{aligned} \tag{2.35}$$

The square brackets indicate that the integrals are computed at the retarded time $\tau = t - \frac{r}{c_0}$. When integrating along a wall the terms $p'_T(\mathbf{x}, t)$ and $p'_L(\mathbf{x}, t)$ are often referred to thickness and loading terms because of their physical interpretation, this is also the reason for the subscripts. In Equation (2.34) M is the Mach number, the subscripts denotes that an inner product has been taken between the subscripted variable and the subscript where r is the unit vector in the radiation direction and n is in the wall normal unit vector.

2.5 Optimization

Heeds is the optimization program which is used in the project. There are several different optimization algorithms available in Heeds, the recommended algorithm is SHERPA. SHERPA is a hybrid and adaptive algorithm. That the algorithm is hybrid means that it employs multiple search methods at the same time. By doing

this the algorithm uses the best attributes from each search method to make the search more effective. SHERPA also uses global and local search methods. That the algorithm is adaptive means that it adapts itself to the design space as the optimization process is running to be more efficient.

A more thorough description of the theory behind SHERPA is unfortunately not available as it is the trade secret of Heeds.

3

Method

In this chapter the methodology is presented. First the geometry together with the geometry modifications are presented. The chapter continues with the meshes for both the aerodynamics and aeroacoustics simulations. The methodology and case setup for aerodynamics and aeroacoustics follow. The final section of the chapter consist of the joint optimization between the aerodynamics and aeroacoustics.

3.1 Geometry

A full scale model of an SUV is used in the project. In order to reduce time and complexity of the simulations a flat floor is used. Gaps in the geometry such as the front grille and the wheel housings are also closed for the same reason. The pre-processing program ANSA is the program that is used to modify the geometry. The model can be viewed in Figure 3.1.

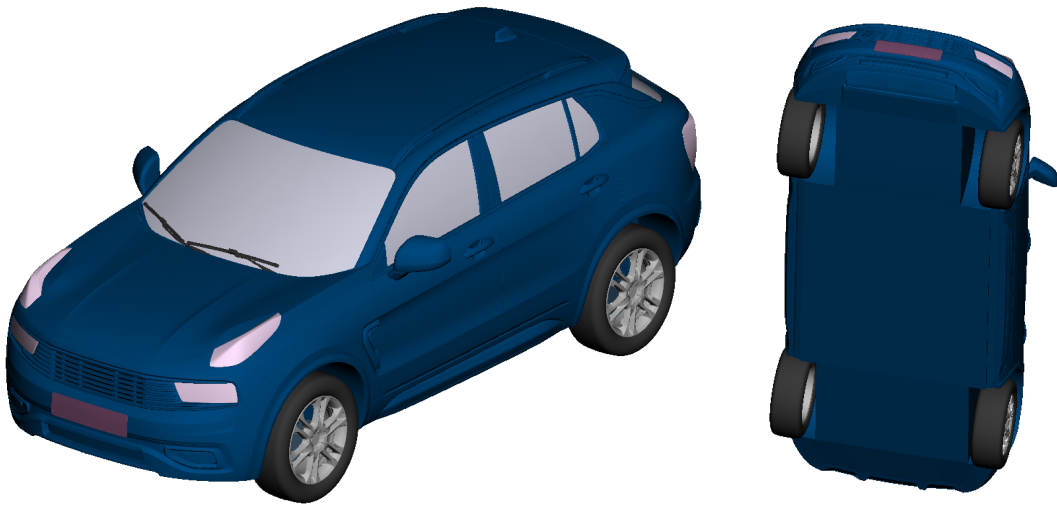


Figure 3.1: Full scale ANSA model of the car with flat floor and completely closed at grille, wheel housings etc.

Two different parameters for the side mirrors are modified. One parameter is the position along the vehicle. The span that is tested is between moving the mirror 100 mm backwards and 100 mm forwards. The positive direction of the parameter is defined as forward on the car. The full span might not be feasible as the driver is required to see the mirrors well but the span is chosen in such a manner to get a

3. Method

better understanding of the parameter and its volatility. The baseline and the two extremes can be observed in Figure 3.2.

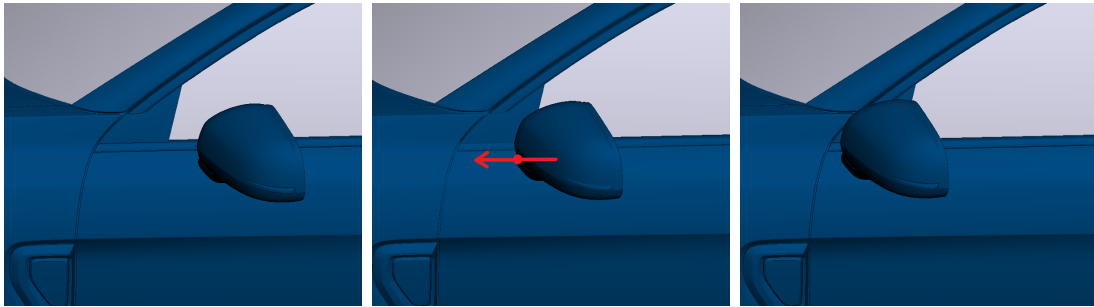


Figure 3.2: Modifications of the side mirror position along the vehicle. The first picture corresponds to -100 mm, the middle is the baseline model and the last picture corresponds to 100 mm.

The second parameter is the diffuser angle of the side mirror which is the angle between the inner side of the side mirror and the vehicle itself. The morphing can not be performed by making a parameter specifying an angle. However, a distance can be specified. The distance parameter is in the interval -100 mm to 100 mm and is defined as moving the red dot in the middle picture in Figure 3.3 along the red line. The pictures in Figure 3.3 correspond to 100 mm for the first picture, 0 mm for the middle picture and -100 mm for the last picture. All designs within the span are probably not feasible, especially the designs that shrink the mirror as they reduce the vision on the sides of the car for the driver. However, as for the x-position, the span is chosen with such extremes to get a better understanding of the parameter and its volatility.

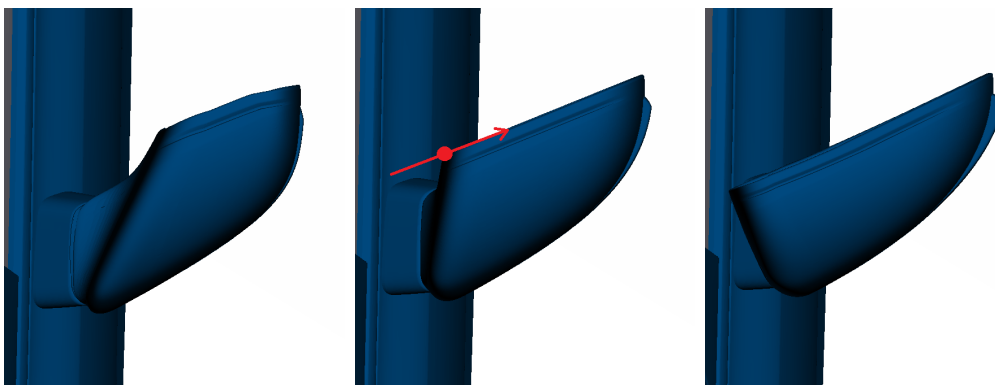


Figure 3.3: Modifications of the diffuser angle of the side mirror. The picture in the middle is the baseline model and the other two pictures are the two extremes in the design space.

The way the modifications of the geometry are done is through the use of morphing boxes in ANSA. Morphing boxes work in the way that the geometry within the morphing box follows and scales with it. For example if you have a rectangular box and you half the size in one direction the entire geometry inside the box will

be squeezed together into half the size, or if you move the box the geometry moves with it. Symmetric morphing boxes are used to get identical changes to both side mirrors. When the morphing boxes are set up, the morphing that is desired can be parameterised in order to easily be changed. By parameterising it is possible to morph the geometry through scripts which enables the geometry modifications to be carried out automatically during the optimization process.

3.2 Aerodynamics

In the aerodynamics simulations the full car is simulated. The domain is 18 car lengths in the flow direction (x-direction), 11 car widths in the y-direction and 9 car heights in the z-direction. The vehicle is placed so that the domain stretches 5 car lengths in front of the vehicle, 12 car lengths behind it and that there is equal spacing on either side in the y-direction, see Figure 3.4. In the z-direction the ground plane cuts through the tires at roughly 20 mm in the z-direction in order to simulate having a contact patch with the ground.



Figure 3.4: The computational domain for the aerodynamics simulations.

3.2.1 Mesh

The computational mesh for the aerodynamics simulations is initially a hexa core mesh with 21 million cells. The mesh consists of six bodies of influence (BOI) in the shape of the vehicle surrounding the vehicle with different cell sizes, these BOIs can be observed in Figure 3.5. The mesh is also adapted in the near wall region with 16 prism layer cells which gives the final mesh with a total cell count of 47 million cells. The near wall adaption is done so the first computational cell has a $y^+ < 5$. Ideally the first cell would have a $y^+ \approx 1$ although $y^+ < 5$ is acceptable [14]. A growth rate of 1.2 is used for the 16 prism layers. The y^+ of the cells closest to the vehicle can be observed in Figure 3.6.

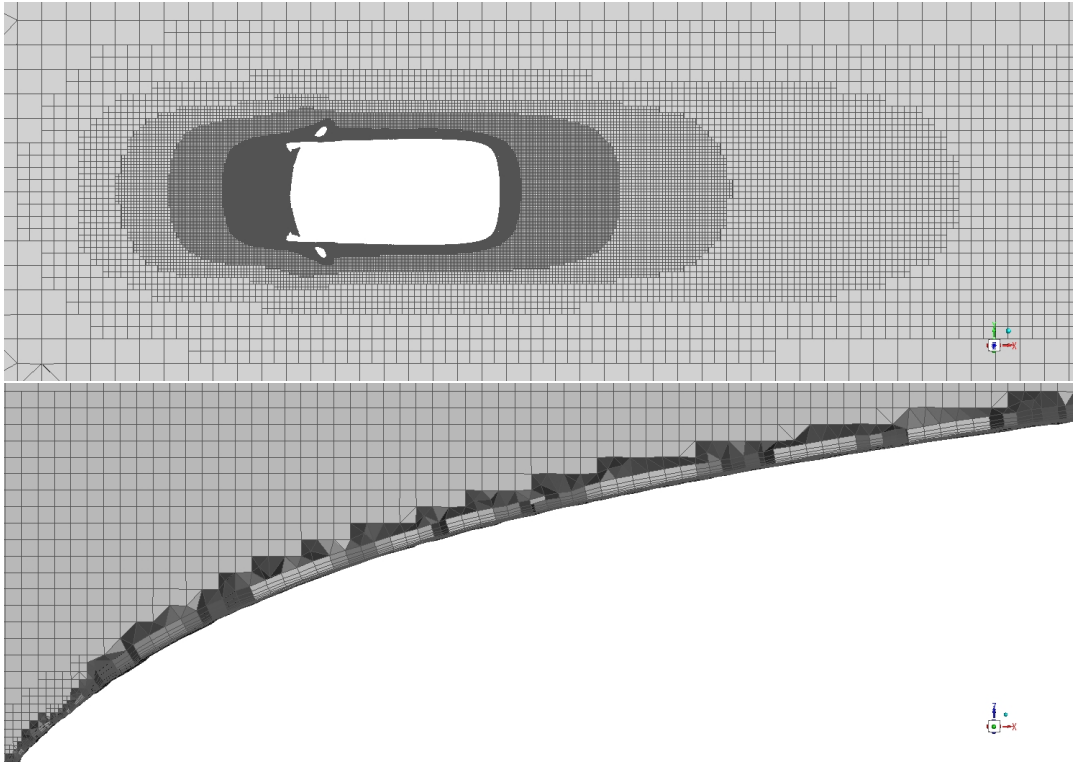


Figure 3.5: The upper picture shows the volume mesh around the vehicle where the BOIs can be identified. The picture is taken at a cut at 1.2 meters above the ground. The lower picture is a zoomed in picture of the hood of the car where the refinement in the near wall region is more prominent. This picture is taken on a plane through the middle of the car.

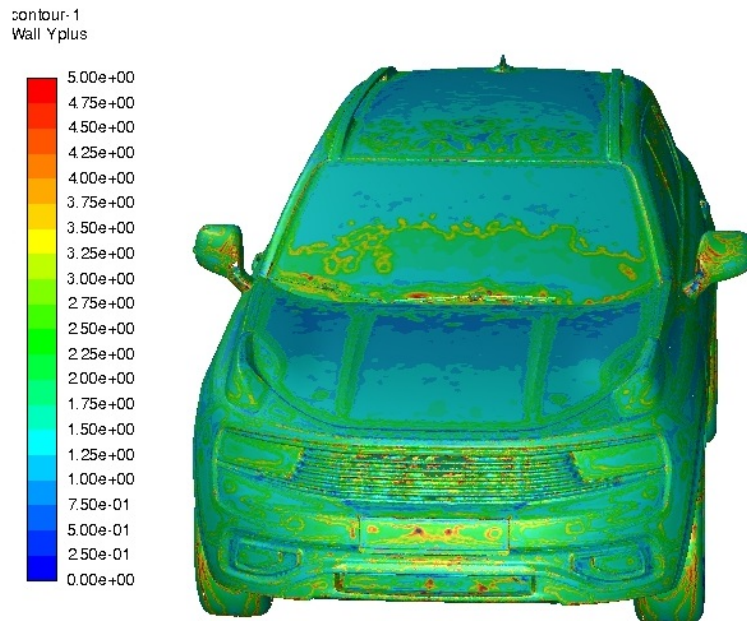


Figure 3.6: y^+ of the cells closest to the vehicle.

3.2.2 Case

The aerodynamics simulations are carried out with a free stream velocity of 27.78 m/s (100 km/h) in the normal direction of the inlet. The entire car has wall boundary conditions and the ground boundary is a moving wall with the velocity 27.78 m/s. The turbulence is modelled using the realizable $k - \epsilon$ which is well suited for external aerodynamics [15]. The enhanced wall treatment option is chosen in FLUENT [14].

3.3 Aeroacoustics

The aeroacoustics simulations are computationally heavier than the aerodynamics simulations. Therefore the domain was reduced for the aeroacoustics in order to reduce the cell count. Half the car is simulated from aeroacoustics with a symmetry plane through the center of the car. The domain was also reduced in the x-direction to 11.5 car lengths, to 3 car widths in the y-direction and 4 car heights in the z-direction. The vehicle is placed so that it the domain stretches 2.5 car lengths in front of the vehicle 8 car lengths behind it. As for aerodynamics the ground plane cuts through the tires at roughly 20 mm in the z-direction in order to simulate having a contact patch with the ground.

3.3.1 Mesh

Just as for aerodynamics the aeroacoustics simulations have a hexa core mesh, initially with 34.5 million cells. In order to reduce the amount of cells the aeroacoustics mesh consists of three instead of six BOIs, see Figure 3.7. Another difference between the meshes is that a refinement region around the side mirror and side window is added which can be observed in Figure 3.8. This refinement is the reason why the initial mesh has more cells for aeroacoustics than for aerodynamics. The mesh is also adapted in the near wall region with 16 prism layer cells as for aerodynamics which gives the final mesh with a total cell count of 51.9 million cells.

The refinement region consist of a rectangular box which extends roughly 200 mm in front of the mirror and 1100 mm behind the mirror. There is also a 200 mm thick refinement on the side window. All cells in the refinement region are hexa core elements with a size of 2 mm in each direction, except for in the near wall region where there are prism layers . The refinement around the mirror can be observed in Figure 3.7 and the refinement region is visualised in Figure 3.8. The refinement is covering the mirror since the small changes to the flow that comes from the changes to the geometry are better captured with the finer mesh. The mesh is also covering the side window because the acoustic sampling will take place on the window.

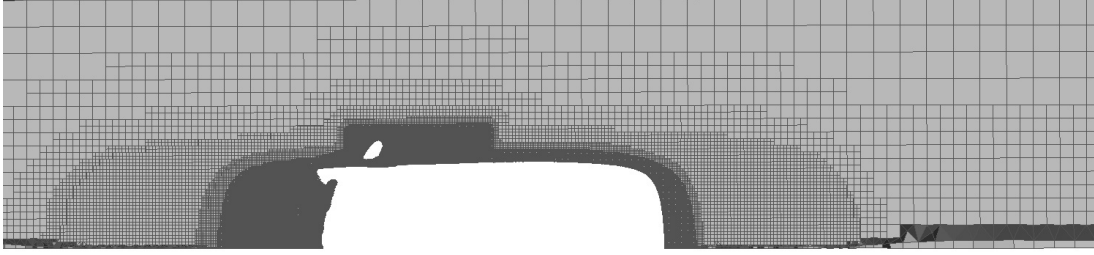


Figure 3.7: The figure shows the volume mesh around the vehicle for the aeroacoustics simulations. Note the refinement box around the side mirror.

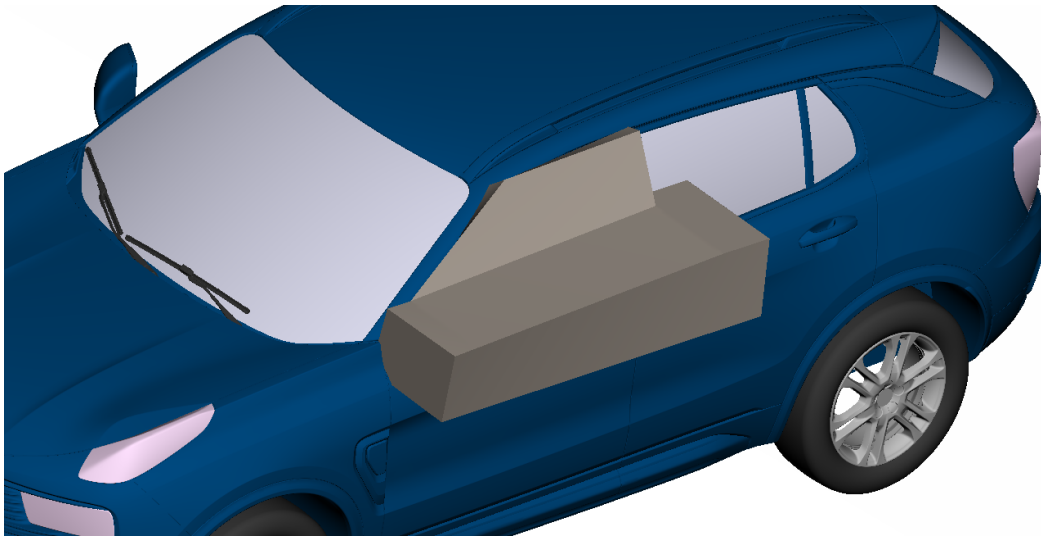


Figure 3.8: The grey region shows the region where the mesh is refined in the aeroacoustics simulations.

3.3.2 Case

To get a larger influence on the sound level, the free stream velocity is set to 38.89 m/s (140km/h), in the normal direction of the inlet, instead of 27.78 m/s as for aerodynamics. The entire body of the vehicle has wall boundary conditions and the ground boundary is a moving wall with the velocity 38.89 m/s. The turbulence is modelled with the DDES approach. The WALE model is used in the LES region and the SST $k - \omega$ model in the RANS region. All coefficients are chosen as default in the software, see ANSYS FLUENT user guide [14]. Second order upwind schemes are chosen for the convective fluxes and an implicit second order scheme is used for the time discretization.

The simulations are first run for 0.101 seconds, which is equivalent to the air flowing through the refinement region three times, in order to reach a statistically steady state. After the statistically steady state was reached the sampling was done with a time step of $3 \cdot 10^{-5}$ for 0.0375 seconds. The results in terms of SPL was taken for the octave bands with frequencies 125, 250, 500 and 1000 Hz. See Appendix A for reasoning behind the simulation times and sampling frequencies.

The source surface for the FW-H analogy is the side window and no receivers are specified. The sampling could have been done on the side mirror with receiver points placed on the window. However the parameters that are investigated are expected to influence the flow on the side window and cause bigger noise differences between designs than the approach with noise generation on the mirror.

3.4 Optimization

The software that is used for the optimization is called HEEDS. To run HEEDS all that is needed is to specify the input parameters, the output parameters and a bash script which will be run. The two input parameters are the morphing parameters specified in Section 3.1. Both parameters have a resolution of 21 which means that the possible choices of both parameters span from -100 mm to 100 mm with 10 mm increments. The total amount of possible designs is 441. The two output parameters that will be minimised are the drag coefficient averaged over the last 50 iterations and the SPL when adding the sounds of the different octave bands together.

The bash script run in HEEDS starts ANSA with the model of the car including the morphing boxes. When ANSA is started the morphing is done according to the input parameters decided by HEEDS and the surface is meshed. After the surface mesh is created FLUENT is started and the surface mesh is loaded. When the mesh is loaded the volume meshing begins. This is done for aeroacoustics and aerodynamics simultaneously. Once the meshing is completed the simulations start. When both simulations have finished the averaging of the drag coefficient and the computation of the total SPL is carried out. HEEDS reads these outputs and chooses new input parameters based on the chosen optimization algorithm. SHERPA is the optimization algorithm used in this project. When the new parameters are chosen the process starts over. The work flow is shown in Figure 3.9.

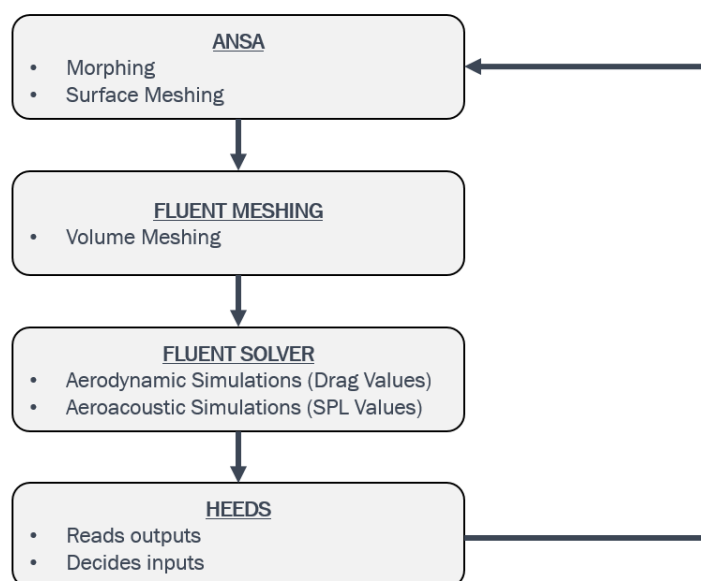


Figure 3.9: Optimization work flow.

3. Method

This optimization loop continues for the amount of evaluations you have given or until you meet any other stopping criteria you have chosen such as if the drag coefficient is below a certain value. In this project the optimization loop is run for 10 evaluations and no addition stopping criteria is used. This number is not enough to get a good optimization of the parameters. To get a good optimization a minimum of 30 evaluations are needed and that is simply not feasible with the computational power at our disposal. However, the project is mainly about the process and the work flow of the optimization and simulation method and not about the exact optimized mirror.

4

Results and Discussion

In this chapter the results are presented and discussed. The optimized design obtained from HEEDS is presented first. The results from the aerodynamics simulations follow together with comparisons between the optimized design and the baseline model. The chapter continues with a section of the aeroacoustic results from the optimized design and the baseline, together with comparisons. A discussion about the in and output parameters and an overview of the other designs conclude the chapter.

4.1 Optimized design

The results corresponding to optimized design is presented in Table 4.1. The first two columns are the design parameters, the third and fourth columns are the optimization parameter ratios and the last column is a performance parameter. The drag coefficient and the SPL ratios are calculated as the value from the simulated design divided by the value of the baseline. The performance of an arbitrary design i is calculated as the sum of the two ratios,

$$Performance_i = \frac{Cd_i}{Cd_b} + \frac{SPL_i}{SPL_b},$$

where the subscript i indicate the design that is observed and b indicate the baseline design. The optimized design is the design with the lowest performance. For the number of simulations that were run the optimized design was the design for which the mirror was moved 100 mm forward and the diffuser angle was made slightly larger.

Angle	X-position	C_d ratio	SPL ratio	Performance
0	0	1	1	2
30	100	0.9751	0.9968	1.9719

Table 4.1: The results for the baseline and optimized design from the optimization process in terms of the drag coefficient, combined a-weighted SPL and performance.

4.2 Aerodynamic results

The pressure coefficient, normalized by the maximum value, on the surface of the left side mirror of the vehicle of the baseline model and the optimized design can be observed in Figure 4.1.

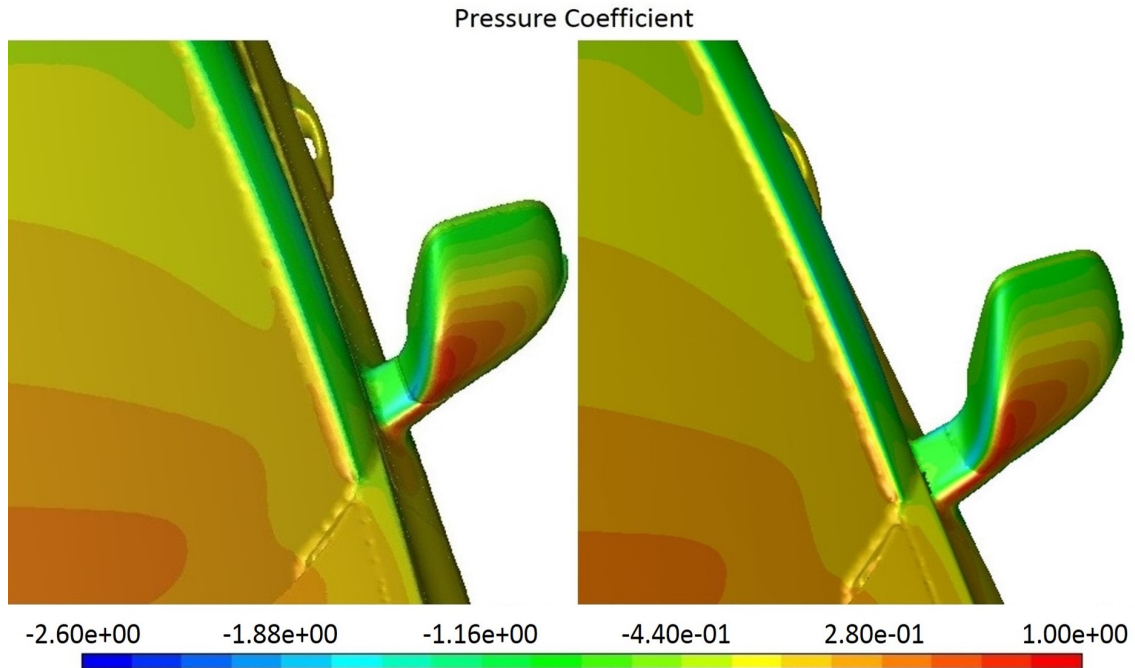


Figure 4.1: Pressure coefficient on the surface of the vehicle normalized by the maximum value, baseline to the left and optimized design to the right.

The front area of the mirrors have a high pressure coefficient and the more perpendicular the area is to the free stream the larger the coefficient is. This is a consequence of the low velocities in these areas which increase the pressure. There are also small areas along the bottom and on the inside of the mirror with a small pressure coefficient. The reason for the small coefficient is the high velocity generated there from the acceleration of the flow around the mirror. In Figure 4.1 it is shown that the pressure coefficient on the inside of the mirror is roughly the same for both designs. Judging by this the flow is attached on the inside of the optimized mirror as it is known that the flow is attached for the baseline from previous simulations. Since the diffuser angle is increased for the optimized design the back area behind the mirror is decreased. Hence is the wake behind the mirror smaller because the flow is attached until it reaches the back of the mirror. A smaller wake behind the mirror means a smaller area of low pressure behind the mirror which in turn leads to a lower drag force.

The normalized total pressure is shown on a plane through the middle of the mirror for the baseline and the optimized design in Figure 4.2.

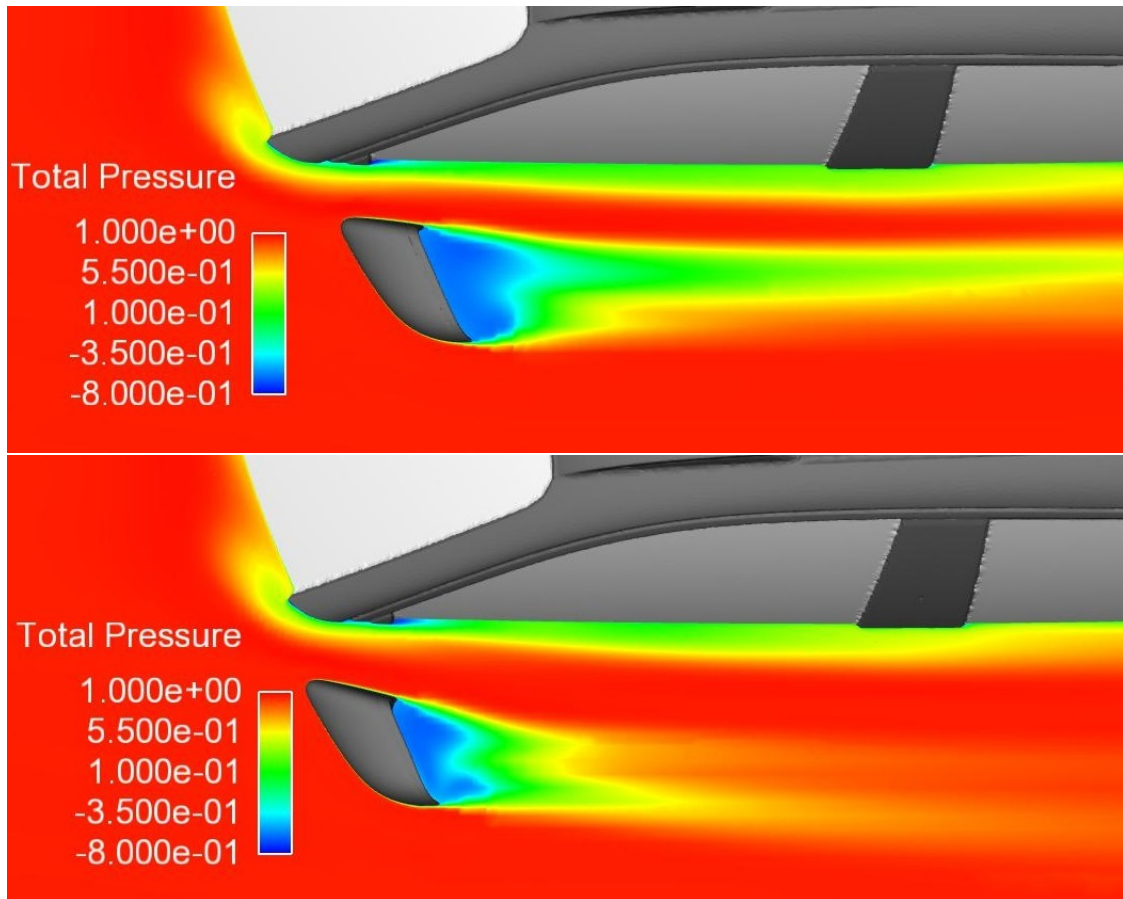


Figure 4.2: Normalized total pressure on a plane through the middle of the mirror for the baseline design (top) and the optimized design (bottom).

It is clear that wakes are generated behind both of the mirrors. However, the wake behind the baseline mirror is larger than the wake behind the optimized mirror. In Figure 4.2 the increased diffuser angle for the optimized design can be observed and how this leads to a smaller back area of the mirror. The high pressure along the inside of the mirrors indicate that the flow is attached for both designs. As was said for the pressure coefficient, if the back area is smaller and the flow is attached until it reaches the back of the mirror the wake will be smaller which is seen in the image.

In Figure 4.3 the vorticity in the range of 0 to 3500 $1/s$ on an iso-surface of total pressure equal to zero for the baseline model and the optimized design can be observed.

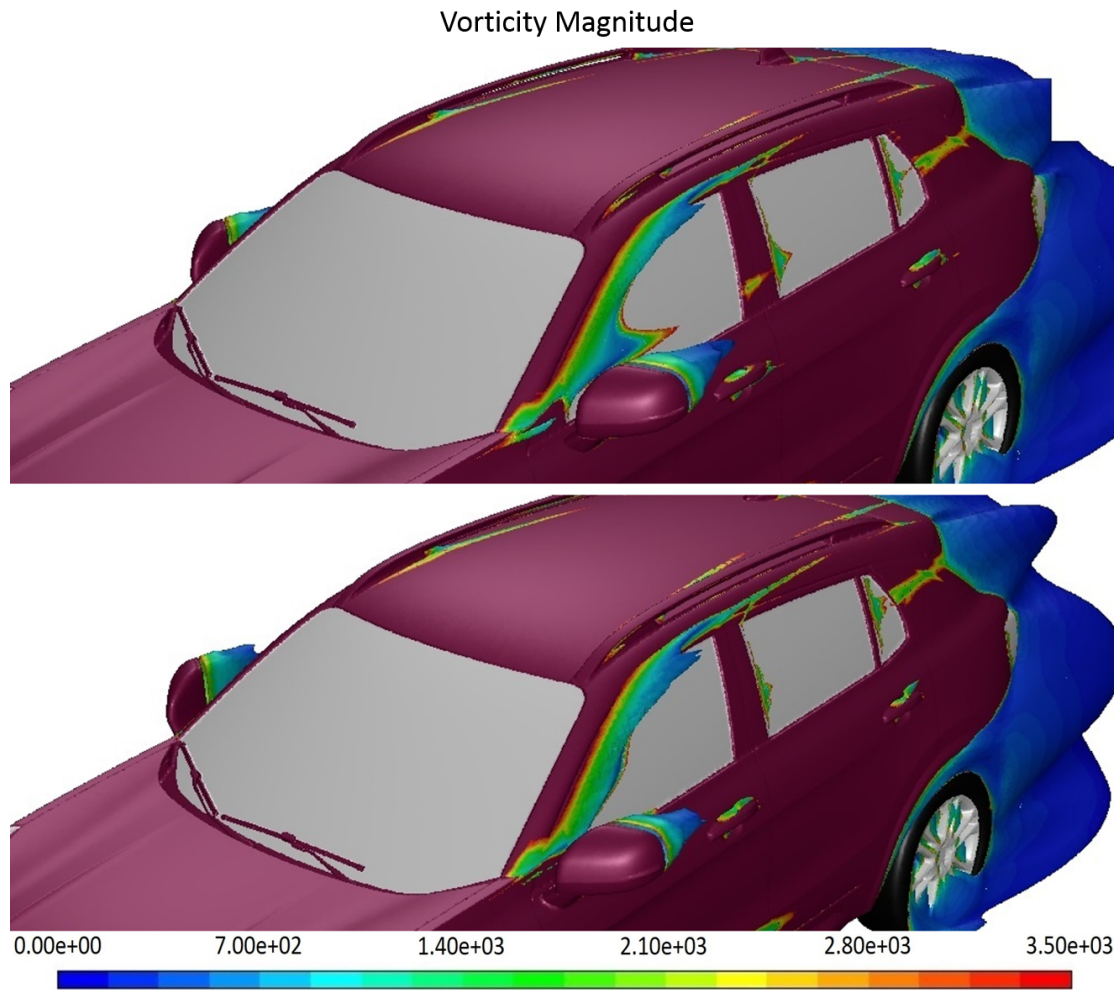


Figure 4.3: Vorticity in the range of 0 to 3500 1/s on an iso-surface of total pressure equal to zero.

The side mirror is a bluff body and is hence creating a wake behind itself. The wake behind the mirror for both designs can be observed in Figure 4.3 and the wake for the optimized design is smaller than for the baseline. The wake behind the mirror, as for the whole car, is characterised by low pressure which increase the drag force acting on the car. The figure also shows a larger vorticity on the inside of the mirror for the baseline. This is due to the smaller space between the mirror and the car itself for the baseline compared to the optimized design. The smaller space leads to larger acceleration and larger velocities which will make for more turbulence and more vorticity. The larger space between the mirror and the car for the optimized design is mainly due to that the mirror is moved 100 mm forward but also from the increase in diffuser angle.

The velocity streamlines around the baseline and the optimized design mirrors can be observed in Figure 4.4.

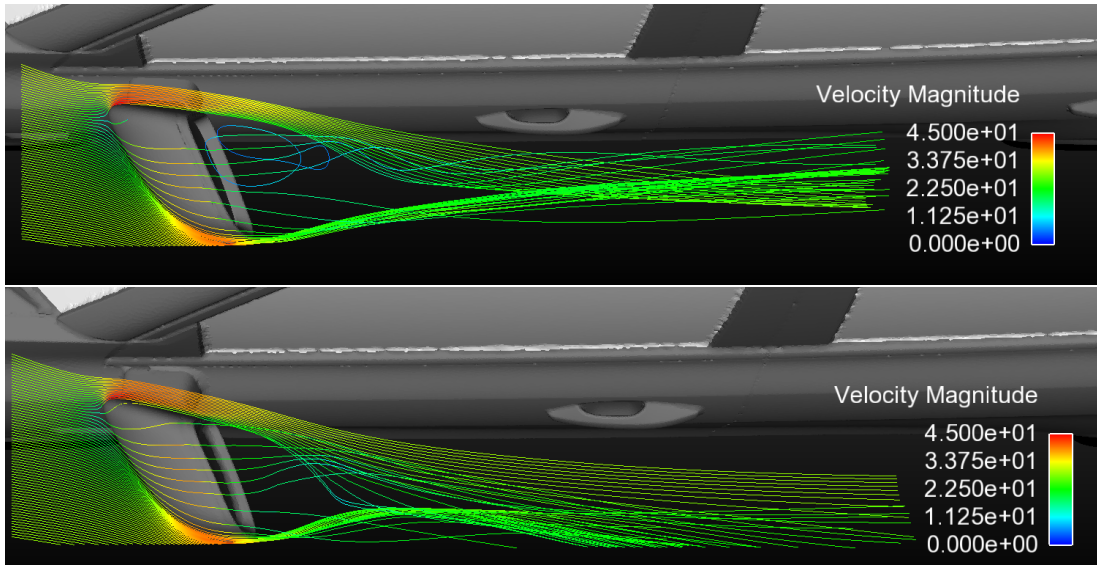


Figure 4.4: Velocity streamlines around the mirror for the baseline (top) and the optimized design (bottom).

As can be judged by the colours in Figure 4.4 the velocity upstream and roughly a meter downstream of the mirror is similar. The velocity is close to 27.8 m/s which is the free stream velocity in the aerodynamics simulations. It can also be observed that there is a wake region directly behind the mirror with low and irregular velocity. The largest velocities are attained at the outer edges of the mirror as the flow accelerates around it. The low pressure in the wake behind the mirror can also be seen in the image as the streamlines turn into the wake as they flow around the mirror. The flow is attached to the inside of the both mirrors and hence is the wake smaller for the optimized design since the back area is smaller.

4.3 Aeroacoustic results

The area averaged, a-weighted SPL values over the front side window for different octave bands and the combined a-weighted SPL are shown in Table 4.2. The values are normalized by the SPL for the baseline in the 1000 Hz frequency band.

Frequency	Baseline	Optimized Design
125	0.8382	0.8600
250	0.9353	0.9375
500	0.9890	0.9871
1000	1.0000	0.9971
Combined SPL	1.0278	1.0260

Table 4.2: Area averaged, a-weighted SPL values over the front side window for different octave bands normalized by the SPL for the baseline in the 1000 Hz frequency band.

When calculating the SPL the logarithm with base 10 is taken of the pressure.

Hence can a small difference in SPL between two different sounds still mean a big difference in pressure. Since the combined SPL is calculated by summing the pressures, a sound with a bigger SPL has a much greater impact on the combined SPL than a source with a smaller SPL. For example is the combined SPL of 10 sounds with an SPL value of 90 each perceived as loud as one sound with SPL 100. This is the reason why the combined SPL is lower for the optimized design than for the baseline design even if the baseline has a lower SPL for frequencies 125 and 250 Hz. The baseline design has slightly larger SPL values for the frequencies 500 and 1000 Hz and since the SPLs are largest for these frequencies they have a greater impact on the combined SPL. Hence is the combined SPL larger for the baseline design than for the optimized design.

Normalized SPL plots for the frequencies 125, 250, 500 and 1000 Hz are plotted in Figure 4.5. Note that these are raw SPL values and not a-weighted.

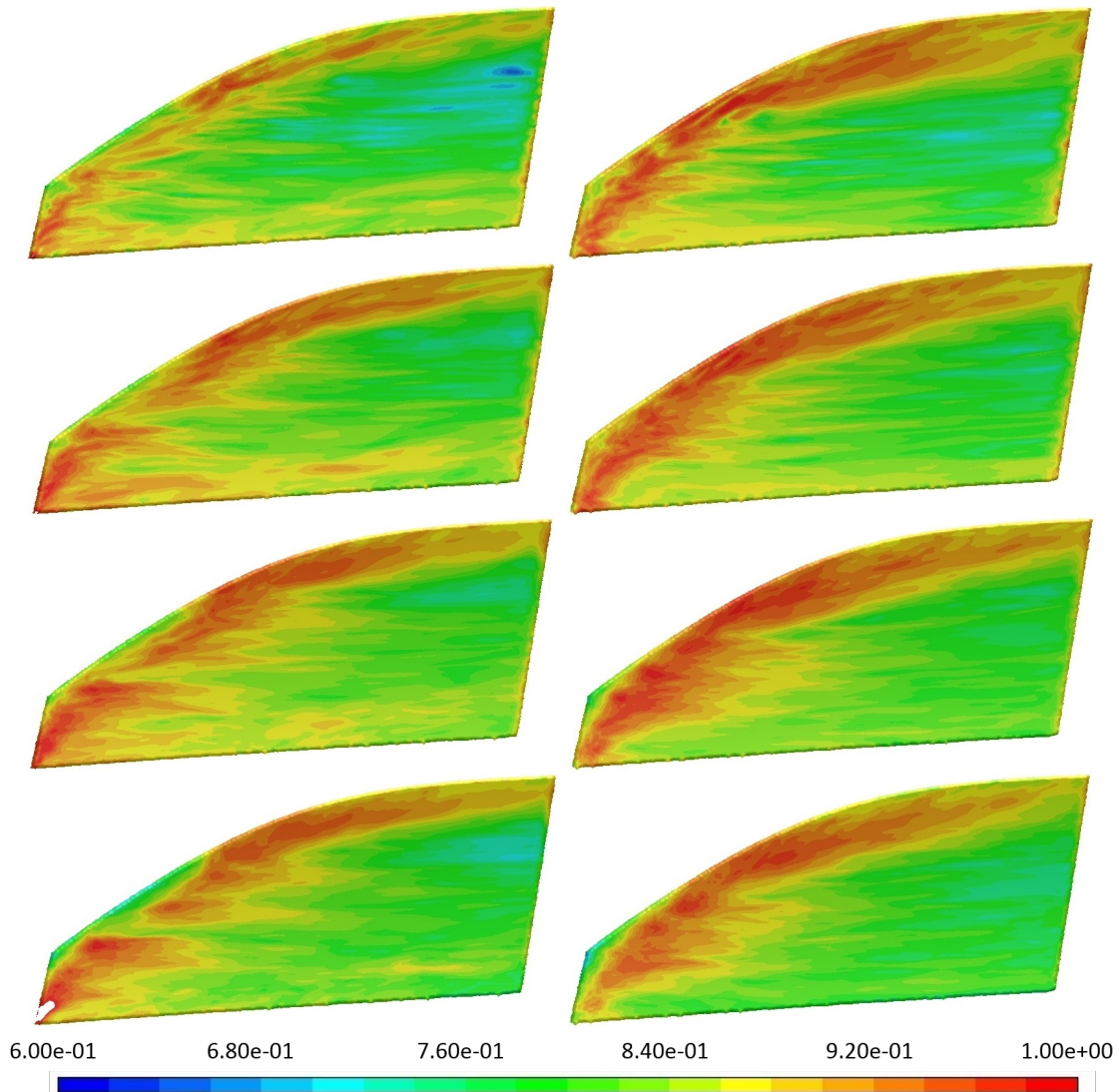


Figure 4.5: Plots of the normalized SPL over the side window. The left images are from the baseline and the right images are from the optimized design. The images are from frequencies 125, 250, 500 and 1000 Hz respectively from top to bottom.

In the first two pictures it is quite clear that the baseline design shows a smaller SPL than the optimized design for 125 Hz. This difference was expected based on the difference between the designs shown in Table 4.2. For the other three octave bands there are no big differences between the designs. The bigger gap between the mirror and the car for the optimized caused less vorticity on the lower part of the window as was concluded from Figure 4.3. This could be the reason why the SPL values are slightly larger for the baseline at the front bottom of the side window compared to the optimized design, especially at the 1000 Hz frequency band.

The vortices over the side window are shown in Figure 4.6 on an iso-surface of the Q-criterion at $2 \cdot 10^6$ coloured by normalized total pressure. The figure illustrates the vortices for the baseline and for the optimized design.

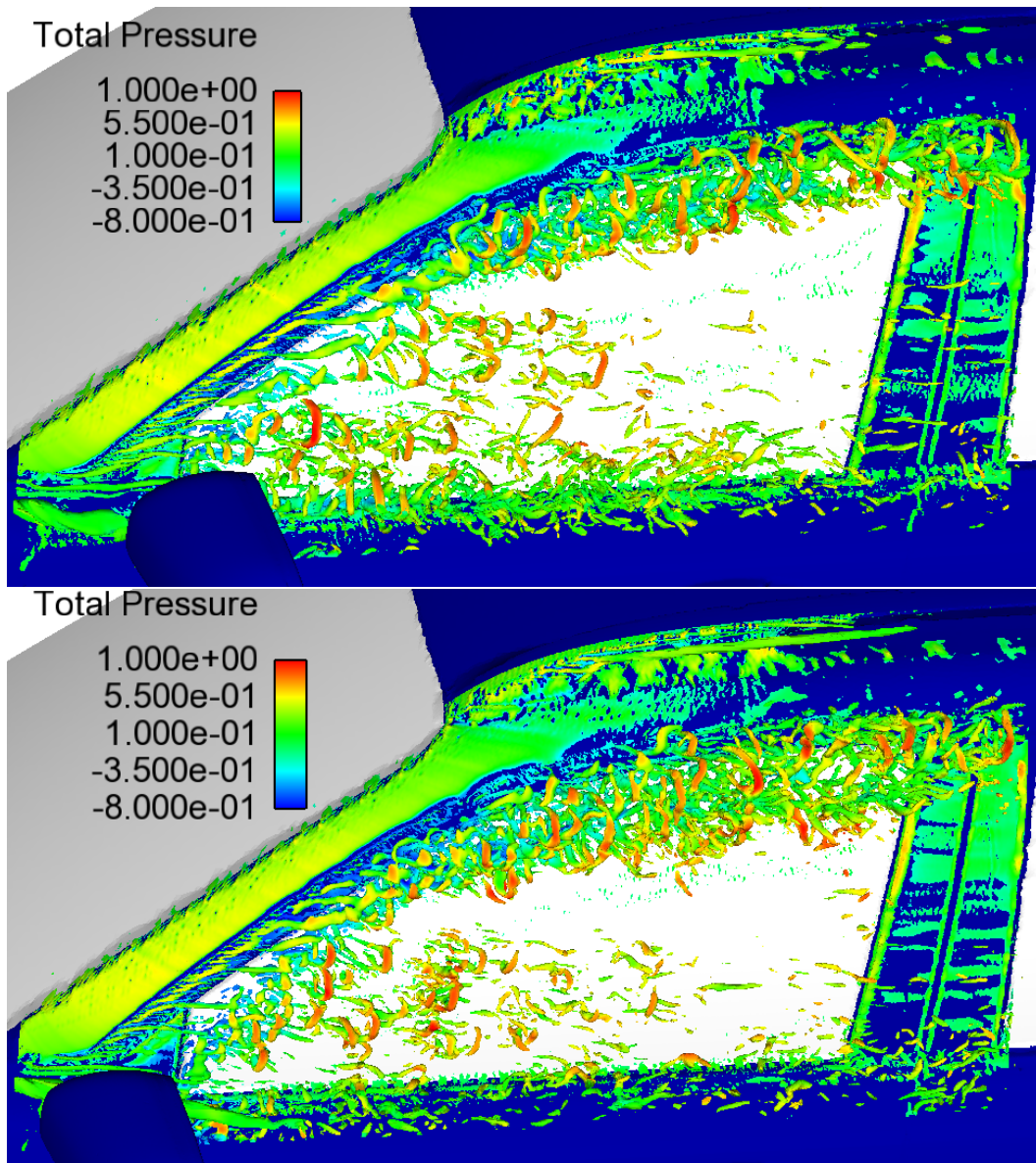


Figure 4.6: An illustration of the vortices over the front side window by an iso-surface of the Q-criterion at $2 \cdot 10^6$ coloured with normalized total pressure. The top image is of the baseline design and the bottom of the optimized design.

The figure shows that there are more vortices at the top of the window and less vortices at the bottom of the window for the optimized design compared to the baseline. This is a reason for the larger SPL values at the top of the window and lower values at the bottom of the window for the optimized design illustrated in Figure 4.5. Less vortices at the bottom of the window can be explained by the larger gap between the mirror and the car as discussed previously. Why there are more vortices at the top of the window for the optimized design compared to the baseline is unclear however. One reason could be that when the mirror is moved forward on the car it has a larger influence on the flow that travels up along the a-pillar which manifest itself as more turbulence and therefore more noise along the top of the window.

4.4 Optimization results

The parameter ratios and performance of all simulated designs are shown in Table 4.3 where the ratios and performance are calculated identically to how it was done for Table 4.1.

Angle	X-position	C_d ratio	SPL ratio	Performance
0	0	1	1	2
30	100	0.9751	0.9968	1.9719
100	-30	1.0133	1.0010	2.0143
-100	30	1.0324	1.0221	2.0545
-30	-30	0.9874	1.0000	1.9874
30	30	0.9855	0.9967	1.9822
100	30	1.0044	1.0021	2.0065
100	-50	0.9925	1.0064	1.9989
-30	10	0.9899	0.9916	1.9815
50	0	0.9864	0.9945	1.9809

Table 4.3: The results from the optimization process in terms of the drag coefficient, combined a-weighted SPL and performance for the different designs simulated.

Most of the simulated designs have a performance in the interval [1.98, 2.02]. This means that when the increase or decrease in C_d and SPL, in terms of percentage points, are summed together the total increase or decrease is less than two percentage points compared to the baseline. The only design that had a better performance than 1.98 was the best design. The only design that had a worse performance than two percentage points was the design with the angle parameter -100 mm and the x-position parameter 30 mm. This design had a performance of 2.0545 where the drag increased by 3.24 percentage points and the SPL on the window increased by 2.21 percentage points. The drag increase is remarkably big for just changing the geometry of the side mirrors. The increase in both disciplines is mainly due to the angle change. The large angle change makes the back area of the mirror larger and will cause a bigger wake behind the mirror, increasing the drag. The angle of the mirror also redirects the flow onto the side window which cause friction on the car

which increase the drag further. The SPL increase also comes from the redirection of the flow onto the side window. As the flow reaches the back of the mirror it will separate and be very turbulent. This highly turbulent flow includes pressure fluctuations which impinge on to the window causing a lot of noise. The large wake and the impingement on the side window can be observed in Figure 4.7.

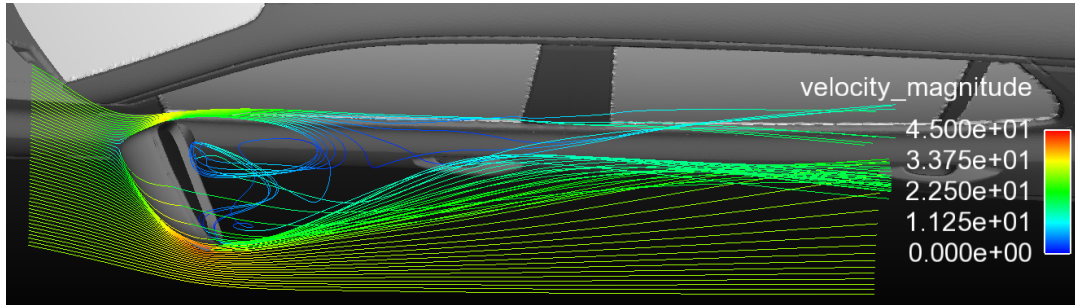


Figure 4.7: Velocity streamlines around the mirror for the worst design.

The correlation between different parameters can be interesting to observe to understand the relation between the different in and out parameters. Table 4.4 below show the correlations between the different parameters in the project. The correlation value is the Pearson correlation coefficient which is a measure of the linear dependency between the variables. Therefore are scatter plots for the five different correlations provided in Appendix B for the reader to see that there is no other apparent dependency between the variables.

	SPL	Angle	X-position
C_d	0.80	-0.25	-0.19
SPL	-	-0.35	-0.07

Table 4.4: The correlation between the different in and out parameters in the project.

The strong correlation between the drag coefficient and SPL is a positive result. It hints that there could be a design which performs well in both disciplines and the designing of the two geometry parameters does not have to be a trade off between drag and noise. Judging by Table 4.3 this does seem to be the case as the design with the best performance has the best performance in drag and second best performance in terms of SPL by a very small margin. The worst design is also the worst design in terms of both disciplines. That the correlations between either design parameter and the two output parameters have the same sign is not a surprise since the correlation between the drag and SPL was strongly positive. The correlations between the design parameters and the output parameters should not be trusted completely. They should only be look at as a rough guide line since both design parameters are changed simultaneously and affect the correlations of each other. However, one could assume that the x-position of the mirror has less of an effect on drag and SPL than the angle since the correlations are less. Increasing the diffuser angle of the mirror slightly should give a smaller drag and SPL value according to the

correlations. This does not have to be true however as the correlations between in and output parameters in Table 4.4 should be taken lightly, especially for the small amount of simulations the correlations are based on.

Performing mathematical evaluations such as curve fitting to a limited data set is not of much value since the results could change heavily with just a few more data points. The results are even less reliable when there are outer factors influencing the data. Which is the case in this project since the two input parameters are change simultaneously. For this reason the results are displayed in Figure 4.8 below where the design space is shown with the designs plotted as bubbles where a larger size means a larger drag coefficient and lighter colour indicate lower SPL.

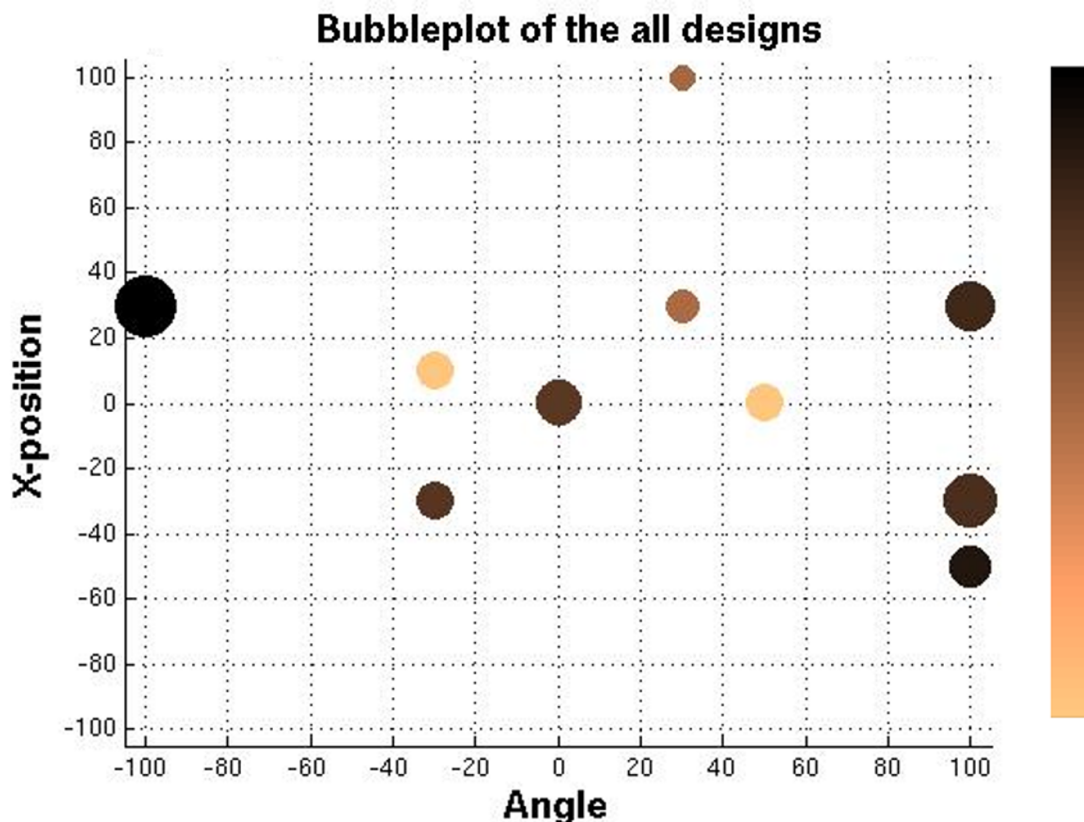


Figure 4.8: Bubble plot showing the entire design space with all design that are simulated. A larger size means a larger drag coefficient and lighter colour indicate lower SPL.

It is clear from the figure that the small number of evaluations left areas of the design space unexplored although some trends can be spotted. The angle parameter seem to be performing best for smaller changes in angle, in terms of drag and SPL. Making the diffuser angle a lot smaller increases the size of wake behind the mirror, which increases drag. An angle decrease also directs more flow towards the window which increase the SPL. If the angle is increased too much the flow is not longer attached to the inside of the mirror. The separation creates a wake behind the mirror which increases drag and when the flow separates it becomes very turbulent which increase the SPL as it impinges on the side window.

It is harder to find any clear trends for the x-position parameter. The designs seem to be performing better, in terms of SPL, when the mirror is moved forward on the car as the four designs with the lowest SPL are for a x-position parameter larger or equal to 0. The drag seems to decrease when the mirror is moved far forward on the car as the two designs with the lowest drag and second lowest drag have x-position parameters 100 and 30 respectively. It should be noted however that 8 out of the 10 designs are within the interval $[-30, 30]$ and the results fluctuate heavily in this interval for the differing angles. For this reason it is hard to draw any conclusions of how the mirror should be moved in the x-direction to lower the drag and SPL.

5

Conclusion

In the project the side mirrors of a passenger car were optimized. Two parameters of the side mirrors were investigated, the position of the mirror along the side of the car and the angle between the inside of the mirror and the car itself. The optimization was done for two disciplines, aerodynamics and aeroacoustics. In aerodynamics the drag on the whole car was considered and the sound pressure level on the front side window of the driver side for the aeroacoustic simulations. The aim of the thesis was to develop a model to run this optimization and also to understand the design parameters.

The main conclusions that were drawn from the thesis were:

- The optimization method using a bash script which incorporates ANSA, FLUENT and HEEDS works as intended and does optimize the output variables.
- The correlation between the drag coefficient and the SPL was high which means that there should be designs that perform well in both disciplines.
- The diffuser angle should be made slightly larger to decrease the size of the wake and direct the flow away from the window. Although not enough to make the flow separate at the inside of the mirror.
- The optimal position of the mirrors along the side of the car did not seem to be inside the investigated interval. However, changing the position of the mirrors outside of the interval is not really feasible as it would be hard for the driver to see the mirrors then.
- In order to truly optimize a part of the car within a reasonable time, changes would have to be made to the set up. Either by observing only one morphing variable, simplifying the simulations or both. The aeroacoustic simulations should perhaps have been done for a mirror over a flat plate in order to reduce the domain and amount of cells.

5.1 Future work

- Validating the simulations with experimental data.
- Refining the mesh to capture sounds with higher frequencies would be interesting. The a-weighted SPL values in the octave band with nominal frequency 2000 was around 95 % of the SPL registered for the band with nominal frequency 1000. This value might be underpredicted as similar simulations were run in [16] and they showed an underprediction of the SPL above the cut-off frequency. If this would be the case it would have an impact on the results.

- Longer sampling time should be used to get a more statistically steady results. Especially for the lower frequencies.
- Because of the reasonable low Mach number incompressibility was assumed and the volume integrals were neglected in the FW-H formulations for the aeroacoustic simulations. The effects these assumptions have on the results should be small according to theory. Although they have not been tested and might be worth investigating.
- More evaluations should be run in HEEDS to get better results from the optimization and more statistics about the parameters.
- There was not enough time to simulate setting the mirror head and foot as acoustic sources and propagating the sound to receivers on the side window. Doing this would give a deeper understanding of how the geometry parameters affect the noise at the side window.

Bibliography

- [1] Hucho, W., et. al. (1987) *Aerodynamics of Road Vehicles*, 1 edn., Oxford: Butterworth-Heinemann Ltd.
- [2] Davidson, L. (2018) *Fluid mechanics, turbulent flow and turbulence modeling*. [Online]. Available at: <http://www.tfd.chalmers.se/lada> (Accessed: 4th May 2018).
- [3] Launder, B. E. and Spalding, D.B. (1974) 'The numerical computation of turbulent flows', *Computer Methods in Applied Mechanics and Engineering* 3(2), pp. 269-289.
- [4] Wilcox, D.C. (1988) 'Re-assessment of the scale-determining equation for advanced turbulence models', *AIAA Journal* 26(11), pp. 1299-1310.
- [5] Speziale, C. G., Sarkar, S., and Gatski, T. B. (1991) 'Modelling the pressure-strain correlation of turbulence: an invariant dynamical system approach.', *Journal of Fluid Mechanics* 227(1), pp. 245-272.
- [6] Menter, F. R. (1994) 'Two-equation eddy-viscosity turbulence models for engineering applications', *AIAA Journal* 32(8), pp. 1598-1605.
- [7] Versteeg, H. K., Malalasekera, W. (2007) *An Introduction to Computational Fluid Dynamics*, 2 edn., Harlow: Pearson Education M.U.A.
- [8] Nicoud, F. and Ducros, F. (1999) 'Subgrid-scale stress modelling based on the square of the velocity gradient tensor', *Flow, Turbulence and Combustion* 62(3), pp. 183-200.
- [9] Oettle, N. and Sims-Williams, D. (2017) 'Automotive aeroacoustics: An overview', *Journal of Automobile Engineering* 231(9), pp. 1177-1189.
- [10] Rienstra, S.W. and Hirschberg, A. (2018) *An Introduction to Acoustics*. [Online]. Available at: <https://www.win.tue.nl/sjoerdr/papers/boek.pdf> (Accessed: 15th May 2018).
- [11] Lighthill, M. J. (1952) 'On Sound Generated Aerodynamically, I. General Theory', *Proceedings of the Royal Society of London. Series A, Mathematical and Physical Sciences* 211(1107), pp. 564-587.
- [12] Curle, N. (1955) 'The Influence of Solid Boundaries upon Aerodynamic Sound', *Proceedings of the Royal Society A: Mathematical, Physical and Engineering Sciences* 231(1187), pp. 505-514.
- [13] Ffowcs Williams, J. E. and Hawkings, D. L. (1969) 'Sound Generation by Turbulence and Surfaces in Arbitrary Motion', *Philosophical Transactions of the Royal Society* 264(1151), pp. 321-342.
- [14] FLUENT User Guide (Version 18.1), ANSYS Inc, 2017.

- [15] Andersson, B., Andersson, R., Håkansson, L., Mortensen, M., Sudiyo, R. and van Wachem, B. (2011) *Computational Fluid Dynamics for Engineers*, Cambridge: Cambridge University Press.
- [16] Ask, J., Davidson, L. (2006) 'The Sub-Critical Flow Past a Generic Side Mirror and its Impact on Sound Generation and Propagation', *12th AIAA/CEAS Aeroacoustics Conference (27th AIAA Aeroacoustics Conference)* Cambridge, Massachusetts.
- [17] Wagner, C. A., Hüttl, T. and Sagaut, P. (2007) *Large-Eddy Simulation for Acoustics*, Cambridge: Cambridge University Press.
- [18] Larsson, J. (2002) *Computational Aero Acoustics for Vehicle Applications*, Gothenburg: Chalmers University of Technology (Licentiate's thesis - Department of Thermo and Fluid Dynamics).
- [19] Ask, J., Davidson, L. (2005) *The Near Field Acoustics of a Generic Side Mirror based on an Incompressible Approach*, Gothenburg: Division of Fluid Dynamics, Dept. of Applied Mechanics, Dynamics, Chalmers University of Technology.
- [20] Bremner, P. and Zhu, M. (2003) *Recent Progress using SEA and CFD to Predict Interior Wind Noise*, 2003-01-1705, SAE 2003 Noise & Vibration Conference and Exhibition.

A

Simulation times and frequency limits

The transient simulation time until the sampling is started is 0.101 seconds, equivalent to the flow going through the refinement region three times. The simulation time should ideally be longer in order to assure statistically steady state. However, since many simulations have to be run for the optimization and the computer power is limited this is the best that can be done within the time frame. Figure A.1 below shows the position of five monitor points on the front side window. Figure A.2 shows the time history normalized total pressure for the five points on the side window for a flow time of 0.5 seconds. The image shows that the flow is at a statistically steady state after 0.1 seconds which makes it acceptable to start sampling.

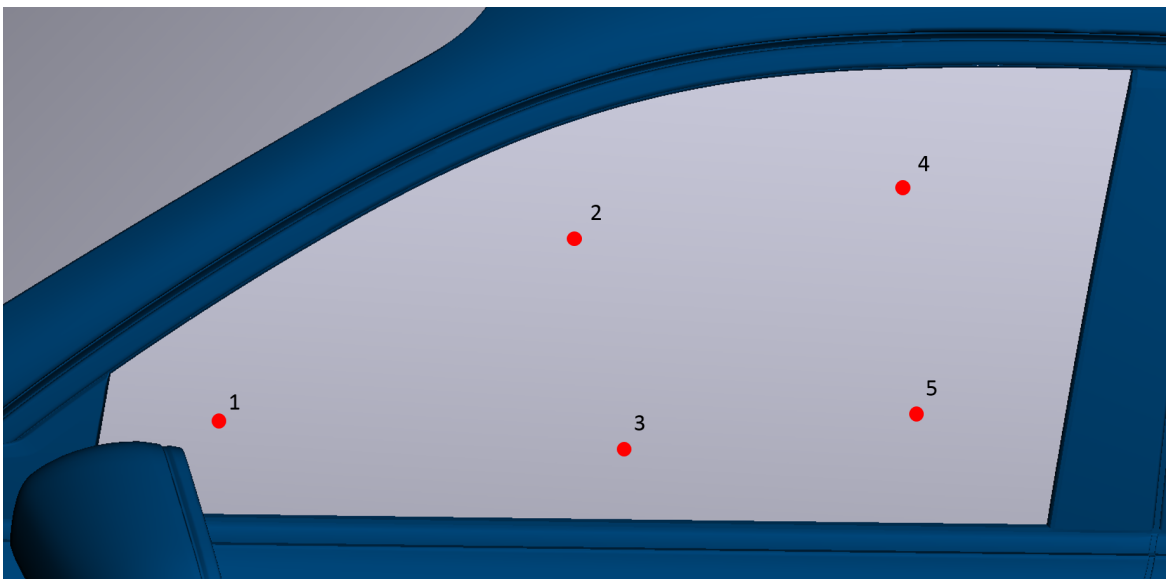


Figure A.1: Positions of the five pressure monitor point on the side window.

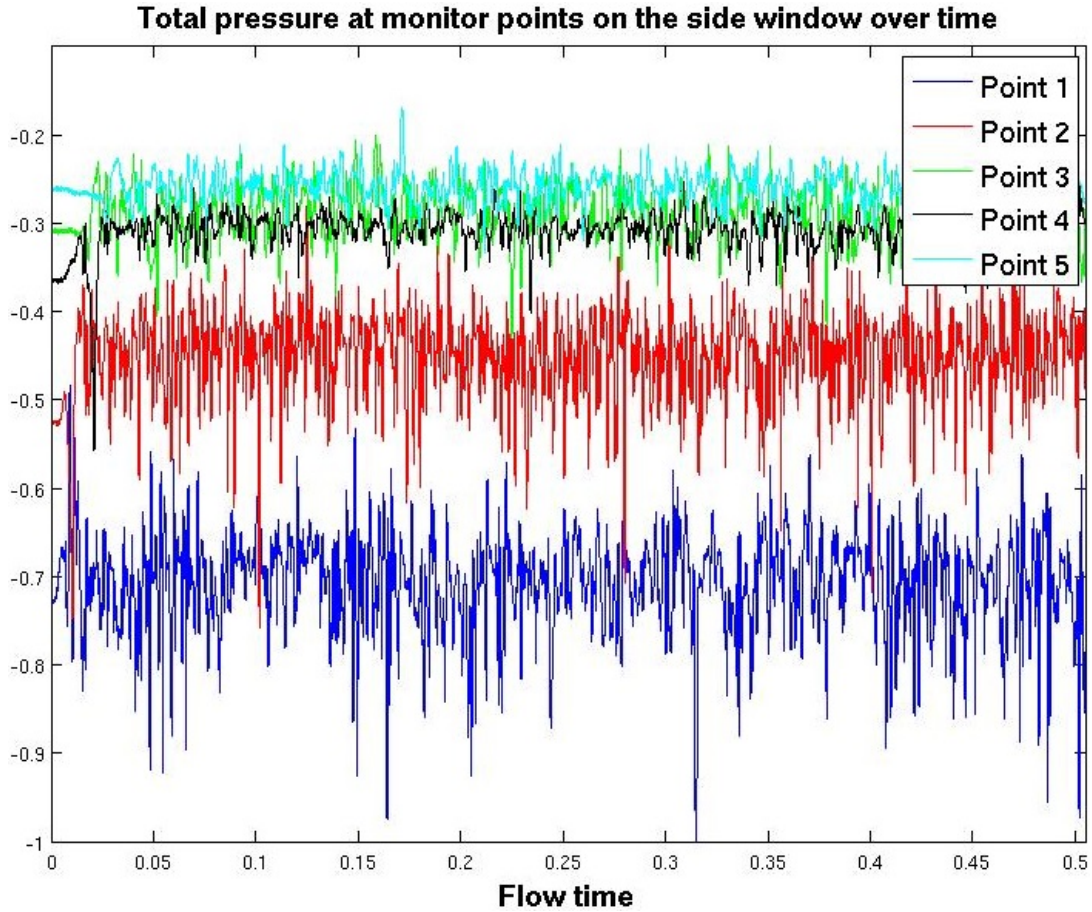


Figure A.2: The normalized total pressure of five points on the side window for a flow time of just over 0.5 seconds.

The results from the octave band with nominal frequency 125 Hz is the lowest frequency that is considered in the aeroacoustic simulations. The reason for this limit is the simulation time. A lower frequency limit would require longer sampling time which is not feasible for this project. The sampling time of 0.0375 seconds means 4.6875 wave lengths of a wave with frequency 125 Hz is covered. Ideally the amount of wave lengths should be more, preferably 10 or more to get a more statistically stable result. Although, the results with ≈ 5 wave lengths should give results accurate enough for this project. The octave band with nominal frequency 63 Hz would only have just above two wave lengths covered in the simulation which is too low in order to trust the results which is why it is neglected. Neglecting the octave bands of frequencies 63 Hz and lower is not much of a loss since these frequencies are weighted down heavily by the a-weighting which would mean that those frequencies have a small impact on the results.

An estimate of the upper frequency that your mesh can resolve is the cut-off frequency. The maximum frequency is computed as $f_{max} = \sqrt{\frac{2}{3}k}/2\Delta x$, [17], where k is the turbulent kinetic energy and Δ is the local grid size. Figure A.3 below shows the cut-off frequency plotted over the source surface. The figure shows that a frequency of 1000 Hz is resolved partly on the source which is the reason why the octave bands above 1000 Hz are neglected. It should be kept in mind when viewing

the results that the frequency 1000 Hz is only partly resolved which means that the results could be slightly less accurate than for the other frequencies.

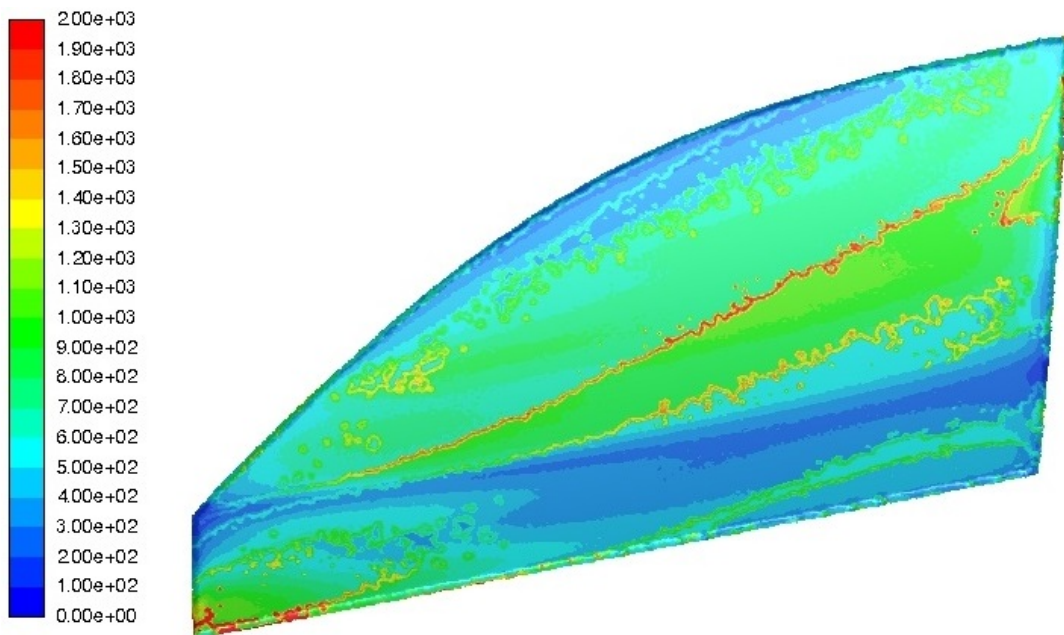


Figure A.3: Frequency cut-off on the front side window, the source surface.

B

Correlation plots

Scatter plots between the inputs and outputs.

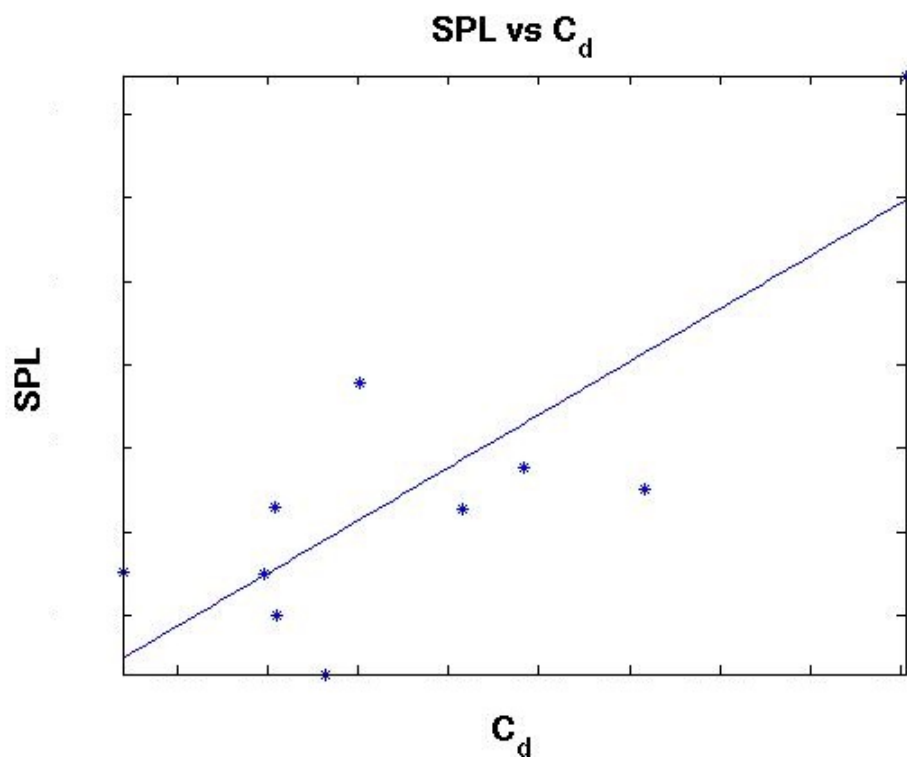


Figure B.1: Scatter plot of the SPL vs the drag coefficient with a fitted linear curve.

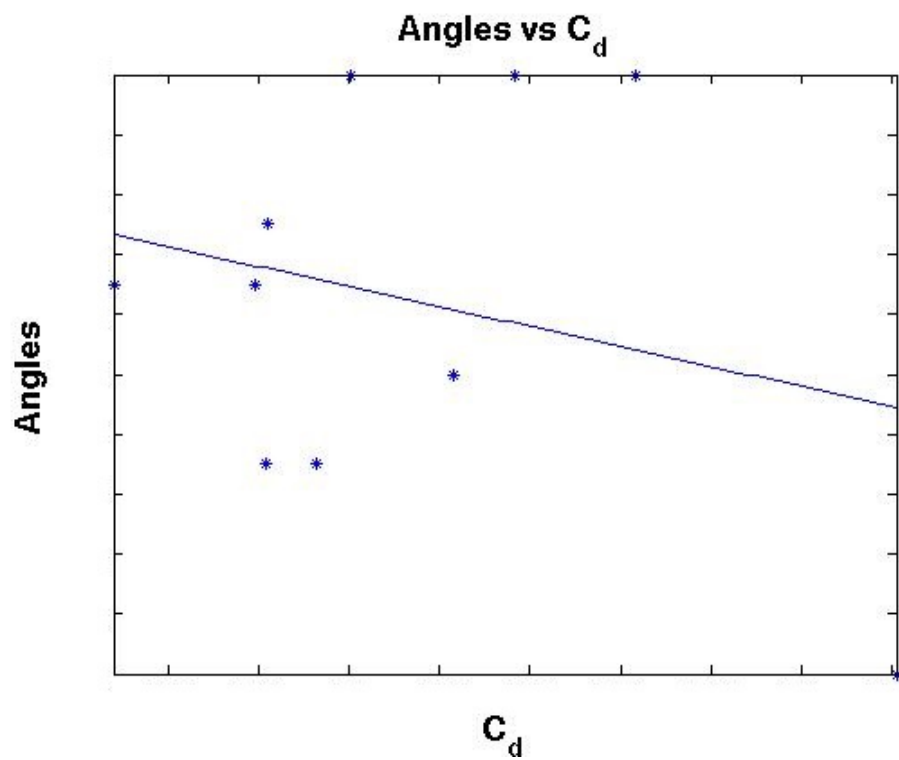


Figure B.2: Scatter plot of the angle parameter vs the drag coefficient with a fitted linear curve.

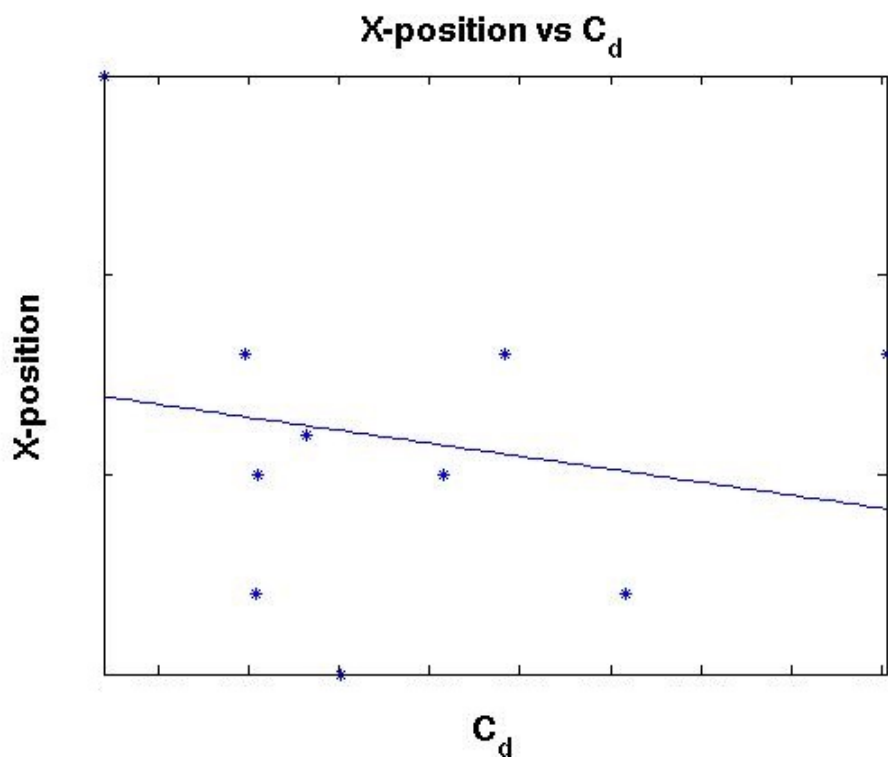


Figure B.3: Scatter plot of the x-position parameter vs the drag coefficient with a fitted linear curve.

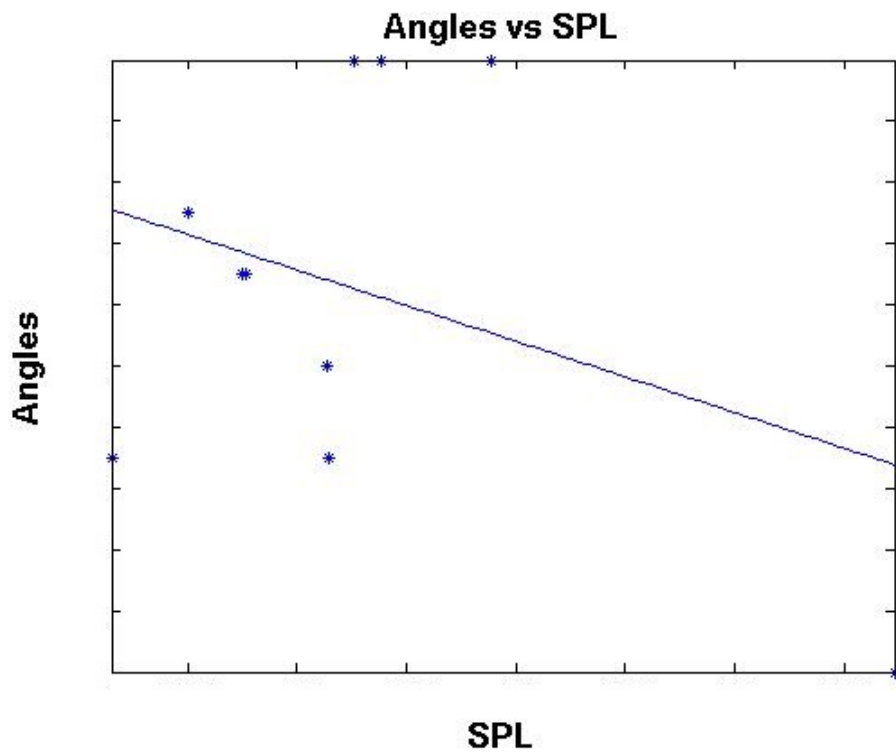


Figure B.4: Scatter plot of the angle parameter vs the SPL with a fitted linear curve.

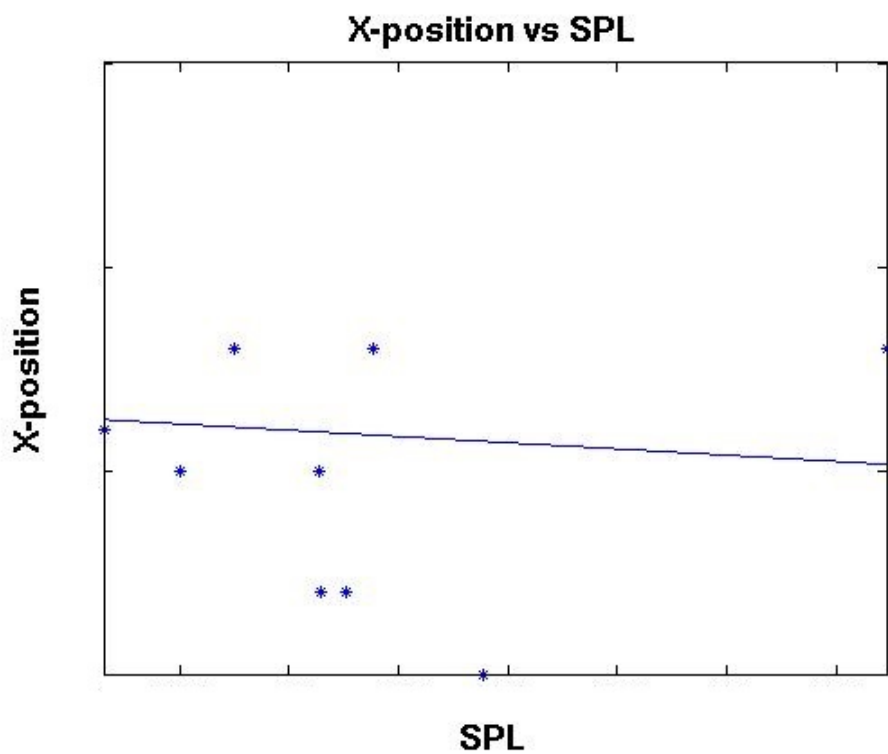


Figure B.5: Scatter plot of the x-position parameter vs the SPL with a fitted linear curve.